PHYSICAL REVIEW D VOLUME 11, NUMBER 9 1 MAY 1975

Study of the A_2: An analysis of the reaction $\pi^- p \to \eta\pi^- p$ and a missing-mass spectrum at 6.0 GeV/c†

D. Underwood,* G. Conforto,‡ and M. A. Kramer§
The Enrico Fermi Institute and Physics Department,
University of Chicago, Chicago, Illinois 60637

A. W. Key
Fermi National Accelerator Laboratory, P. O. Box 500, Batavia, Illinois 60510
and Physics Department, University of Toronto, Toronto 181, Canada

R. M. Mobley‖
Fermi National Accelerator Laboratory, P. O. Box 500, Batavia, Illinois 60510

R. Prepost, D. H. Tompkins,¶ and M. S. Witherell**
Physics Department, University of Wisconsin, Madison, Wisconsin 53706

(Received 4 November 1974)

The reaction $\pi^- p \to X^- p$, $X^- \to \eta\pi^-$, $\eta \to \gamma\gamma$ has been studied in an optical spark-chamber experiment at the Argonne ZGS (Zero Gradient Synchrotron) at a beam momentum of 6.0 GeV/c and with $0.27 \le |t| \le 0.42$ (GeV/c)^2. The $\eta\pi$ mass spectrum contains about 1400 events in the mass range $0.80 < M(\eta\pi) < 1.55$ GeV/c^2, and is dominated by approximately 1000 events of the type $A_2^- \to \eta\pi^-$. No structure is discernible within the A_2 mass spectrum for an experimental resolution of 7.1 MeV/c^2 [16.7 MeV/c^2 FWHM (full width at half maximum)]. A single D-wave Breit-Wigner distribution fits the data with a high confidence level, yielding for the A_2 the parameters $M_0 = 1.323 \pm 0.003$ GeV/c^2 and $\Gamma_0 = 0.108 \pm 0.009$ GeV/c^2. The angular distribution of the decay $A_2^- \to \eta\pi^-$ is analyzed and the resultant density matrix elements have the values $\rho_{11} = 0.45 \pm 0.02$, $\rho_{1-1} = 0.45 \pm 0.04$, and $\rho_{00} = 0.09 \pm 0.04$. All other elements are consistent with zero. Finally, the missing-mass spectrum in the region of the A_2 is presented. A signal of 230 events above background per 5-MeV/c^2 interval is observed at the A_2 peak, with a signal to background ratio of greater than 1:1. A single D-wave Breit-Wigner distribution together with a quadratic background fits the data well, with the parameters for the A_2 being $M_0 = 1.324 \pm 0.003$ GeV/c^2 and $\Gamma_0 = 0.104 \pm 0.009$ GeV/c^2. Both A_2 mass spectra are incompatible with the dipole shape.

I. INTRODUCTION

This paper reports the results of an optical spark-chamber experiment performed at the Argonne National Laboratory to study the reaction

$$\pi^- p \to X^- p ,$$
$$X^- \to \eta\pi^- ,$$
$$\eta \to \gamma\gamma$$

for an X^- mass in the range 1.0 to 1.5 GeV/c^2 and a beam momentum of 6 GeV/c. Some of the results of this experiment have already been reported[1,2] and the data from a later experiment which used the same apparatus to study X^- masses from threshold to 1.1 GeV/c will be presented elsewhere. The recoil-proton distribution has also been analyzed to produce a missing-mass spectrum, the results of which have been published in Ref. 2. A major aim of the experiment was to perform a high-statistics, high-resolution study of the decay $A_2 \to \eta\pi$ in order to investigate the possibility of structure in the A_2 mass spectrum.

The excitement engendered by the discovery of structure in the A_2 mass spectrum started with a series of measurements by the CERN Missing-Mass Spectrometer (MMS) group. The results of this first series of measurements appeared in 1966 and 1967[3] and showed an A_2 mass spectrum, as measured by a recoil-proton spectrometer operating near the Jacobian peak, which could not be fitted well by a single Breit-Wigner resonance shape. (The χ^2 probability for a single Breit-Wigner fit to that data was less than 0.1%.) Reasonable fits were obtained by assuming a narrow dip structure, approximately in the center of the mass spectrum. Subsequently, the "dipole" shape was invented to conveniently parameterize this structure. The implications of split resonance structure are discussed in the review article of Rosner[4] and references found therein.

Next a CERN group performed a series of measurements with a different experimental configuration called the CERN Boson Spectrometer (CBS).[5] The system detected recoil protons near 0° and close to threshold for A_2 production. The evidence for the original CERN A_2 splitting was a combination of data from these two sets of experiments, and showed a narrow dip ($\simeq$20 MeV/c^2 wide) in the A_2 mass spectrum. Furthermore, this group measured the angular distribution for the A_2 decay into pions. This experiment, as well as the majority of subsequent experiments, determined that the spin-parity assignment for the A_2 structure was 2^+, both below and above the split.[6] Additional studies by the same group confirmed this split structure of the A_2 in the $K\overline{K}$ mode and, with less statistical precision, in the $\eta\pi$ decay mode.[7,8]

Since that time, the A_2 has been studied in many experiments, some of which favor the double-peaked shape. However, those experiments with the ability to clearly discriminate between the single- and double-peaked hypotheses have not confirmed the original CERN result.

In 1969–1970, a high-statistics experiment, performed by the LBL bubble chamber group, gave no evidence for the split[9] in the A_2^+ mass spectrum produced via π^+p interactions. Since the original CERN experiment had observed the A_2^-, this gave rise to suggestions that the structure might be isospin-dependent.

Further missing-mass experiments were reported in 1971 which contradicted the original CERN result. Of the missing-mass experiments, that of the Northeastern–Stony Brook (NE-SUNY) collaboration[10] and that of the Indiana group[11] are particularly important as their mass resolutions and beam energies were similar to the CERN conditions. The NE-SUNY group, in particular, had greater statistical precision and an unbiased missing-mass trigger which did not demand a forward-charged decay particle from the A_2. In addition, two experiments which checked the CBS result by studying the A_2 produced at threshold indicated no structure in the A_2 mass spectrum.[12,13]

More recently, the CERN group has presented a reanalysis of their missing-mass data which reduces the statistical significance of the observed split. These data, along with a review of the present situation, are given in Ref. 14. In summary, the totality of measurements investigating structure of the A_2 as seen from missing-mass-type experiments is consistent with a structureless, or unsplit, mass spectrum.

Since the original CERN result, several experiments have investigated the A_2 mass structure as seen in two other decay modes, $K\overline{K}$ and $\eta\pi$. Two experiments,[15,16] although performed at higher beam momenta, but with far superior mass resolution, reported that a single Breit-Wigner function gave a good fit to the $K\overline{K}$ decay-mode mass spectrum.

However, no convincing check on the question of structure in the $\eta\pi$ mode had been presented prior to Ref. 1. The only single experiment in the $\eta\pi$ decay mode with statistics comparable to that of the original CERN data was that of the LBL bubble-chamber group.[9] With less than 200 A_2 mesons decaying into $\eta\pi$, and with a mass resolution of 9.3 MeV/c^2 (half width at half maximum), fits to the mass spectrum with a single Breit-Wigner or a "dipole" shape were not distinguishable (with confidence levels of 33% and 21%, respectively).

The study of a resonant decay into $\eta\pi$ has several distinct advantages. First, the $\eta\pi$ decay mode restricts the resonance to a natural spin-parity sequence. Second, the cross section for nonresonant $\eta\pi$ production in pion-nucleon interactions is small compared to A_2 production and its subsequent decay into $\eta\pi$. The study of the A_2 in this decay mode therefore provides an excellent signal-to-noise ratio compared to the dominant $\rho\pi$ decay modes. It is also of interest to search for "exotic" mesons not predicted by the simple quark model,[17] and specifically to search for possible $\eta\pi$ decay modes of the resonances in the mass range 0.9 to 1.1 GeV/c^2 which have been reported in a variety of experiments.[18] The only effect so far reported in the region of the A_2 is that of a possibly resonant 1^- $\eta\pi$ partial wave at a mass of around 1.25–1.30 GeV/c^2.[19] This effect is studied in the present paper, but the results of a search for mesons in the lower mass range will be reported at a later data.[20]

The beam momentum and t values of the present experiment were chosen to correspond to the Jacobian peak region of the original CERN experiment. Consequently the beam momentum was fixed at 6 GeV/c with a t acceptance in the range $0.27 \leq |t| \leq 0.42$ (GeV/c)^2. In the Jacobian peak, the mass resolution is relatively insensitive to measurement of the recoil-proton momentum. The angles of the beam pion, recoil proton, and decay pion were measured in separate thin-foil optical spark chambers, and the proton momentum was measured in a multiplate range spark chamber. The $\eta \rightarrow \gamma\gamma$ decay, which provides a very clean signature for the required events, was observed by measuring the γ conversion points in a multiplate shower spark chamber. Since the beam and all the final-state particles were observed, a two-constraint (2C) kinematic fit to $\pi^-p \rightarrow \eta\pi^-p, \eta \rightarrow \gamma\gamma$ could be made.

A total of 360 000 pictures were obtained in two runs. 20 000 of these pictures were selected for measurement according to the criteria described in Sec. III, with subsequent fitting yielding about 1400 events in the $\eta\pi$ mass spectrum of which approximately 1000 are examples of the decay $A_2 \to \eta\pi$. About 1000 $\pi^- p$ elastic scattering events from elastic scattering data taken at a beam momentum of 1.1 GeV/c were measured and analyzed in order to check the event reconstruction and error analysis.

II. EXPERIMENTAL METHOD

A. Beam line

A schematic diagram of the beam transport system is shown in Fig. 1. It consisted of two septum magnets, three bending magnets, four quadrupoles, and a momentum-defining collimator. An extra adjustable collimator was used just upstream of the Q1 quadrupole magnet to adjust the beam intensity and to restrict entering particles to the uniform field region of magnet B1.

To minimize beam scattering, a vacuum line was used for the upstream half of the beam and a helium bag for the downstream half. Pions were produced at an angle of 1.3° from a beryllium target 1.27 cm square by 10.2 cm long, placed in the extracted proton beam line I of the ZGS. An extracted beam of 2.8×10^{11} protons per pulse gave a typical π^- beam flux of 1.1×10^5 per pulse, with the momentum collimator set at $\pm0.4\%$. A wire float of the upstream half of the beam was used to determine the setting for B1, the bending magnet which selects the beam momentum. Subsequent kinematic fits to the data indicated that the beam momentum obtained in this way was approximately 0.25% lower than predicted. The calculated values of magnet currents and fields for a 6-GeV/c beam agreed with the wire-float value to about 0.3%. Currents in all magnets were monitored frequently and maintained to within 0.1% of their tuned value. The field of B1, the momentum defining magnet, was maintained constant to within 0.05% by continuous monitoring using an NMR probe.

A multiwire proportional chamber beam-profile monitor[21] placed just upstream of the hydrogen target, i.e., near the final focus of the beam, was used at the time of beam tuning to give a measured profile of the beam. The spot width (full width at half maximum) was 11 mm. A Monte Carlo program called LURCH, which accounted for all geometric factors but assumed constant magnetic fields, was used to study the beam properties. Measurements of the B1 field indicated an inhomogeneity within the beam region of approximately 0.1%. Therefore, the assumption of constant fields was considered reasonable. LURCH gave a non-Gaussian dispersion of 0.94% FWHM, with some position-momentum correlation. This value has been used as the basis for an estimated beam momentum error of 0.4%. (Unless otherwise stated, the errors indicated in this paper correspond to one standard deviation.)

The beam momentum was retuned to 1.1 GeV/c for the study of πp elastic scattering. Subsequent kinematic fits gave a best beam momentum value of 1.1 GeV/c for the elastic scattering events. The magnet currents were monitored to about 0.2%, and the field in the bending magnet B1 was maintained constant to 0.1% using the NMR probe.

B. Target

The liquid-hydrogen target cell was a cylinder 10 cm in length, 4 cm in diameter, with 0.013-cm-thick Mylar walls, covered with 0.0064 cm of thin Mylar superinsulation. The surrounding vacuum container consisted of an aluminum frame with a small circular beam-entrance window of 0.025-cm-thick Mylar, and a 0.038-cm-thick wrap-around Mylar window covering the sides and downstream end.

Since the mass resolution of this experiment depends critically on the amount of liquid hydrogen traversed by the recoil proton, target positioning was considered very important. Therefore, the target center was offset horizontally 0.88 cm away from the proton arm for the first run, and 0.62 cm away for the second run, in order to

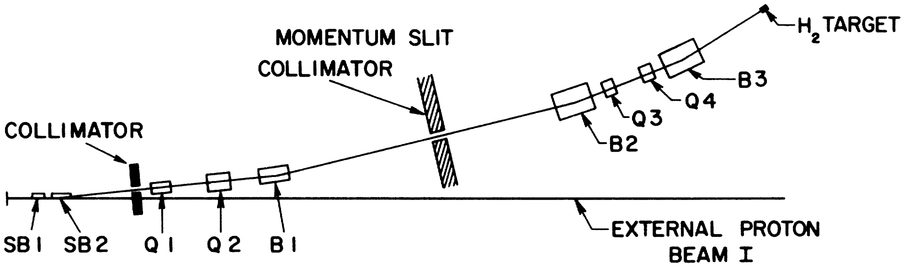

FIG. 1. Schematic drawing of the pion beam line. SB1 and SB2 are septum magnets. Q1, Q2, Q3, and Q4 are quadrupoles, and B1, B2, and B3 are dipoles.

minimize the amount of hydrogen through which the recoil protons traveled. The empty-target trigger rate for the full-trigger condition was typically 20% of the full-target rate. About 25% of the empty-target rate came from the Mylar vacuum window downstream of the cell. Events originating in that window were easily eliminated after a crude vertex reconstruction.

C. Counters, trigger logic, and optical spark chambers

The experimental arrangement sketched in Fig. 2 is an optical spark-chamber system consisting of three main sections: a beam arm, a proton arm set at 58° to the beam (see Table I), and a forward arm set at 7° to the beam to detect the produced γ rays and pions. The counters, electronic logic, and optical spark chambers were of conventional design. The entire arrangement was mounted on a large iron plate which could be pulled out of the beam line.

The first two beam scintillation counters B1 and B2 were 7.62 cm square and 0.016 cm thick. They were placed about 127 cm and 27 cm, respectively, upstream of the hydrogen target and used in coincidence. The beam was further defined by B3, a 15×20-cm veto counter, surveyed onto the beam line just upstream of the target, with a 1.90-cm-diameter hole to pass the beam. A 3.81-cm square beam counter B4, on the beam line 57.2 cm downstream of the target center, was used to veto noninteracting beam particles and thus reduce the accidentals rate. The output of a small counter which intercepted some beam halo at the upstream end of the momentum collimator served to monitor beam intensity, spill time, and beam structure.

The detectors in the proton arm were a multiwire proportional chamber P1 (PWC), a scintillation dE/dx counter, a Lucite threshold Čerenkov counter to veto pions, an angle-defining scintillation counter P2, and a scintillation veto counter P3, placed behind the proton range chamber in order to limit the range of the recoil protons.

The PWC and associated electronics were developed in conjunction with the Enrico Fermi Institute Electronics Shop. Good spatial resolution was not required, the objective being a low-mass counter with good timing resolution and simple reliable operation. The chamber had an active area of 11.9 cm by 12.7 cm with 48 (20-μm) gold-plated molybdenum wires spaced 0.32 cm apart, and a 0.79-cm spacing between the wires and an aluminum foil cathode. Grounded guard rings were situated at the edges of the chamber,

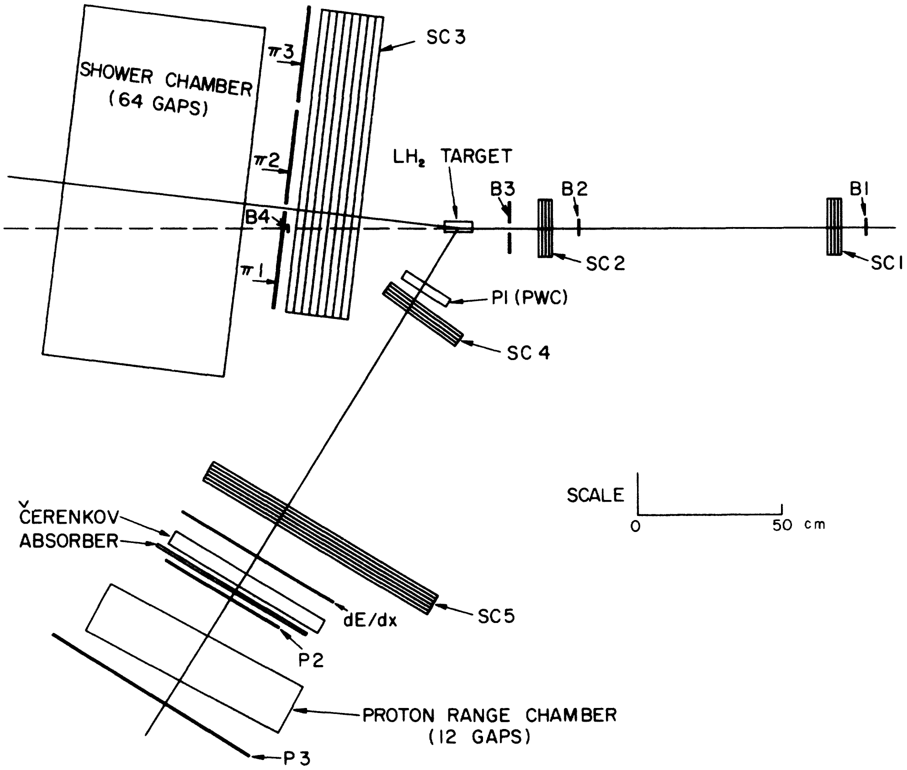

FIG. 2. Plan view of the experimental apparatus.

TABLE I. The thickness of material and distance from the hydrogen target for the proton arm.

Distance from beam (cm)	Material	Thickness (cm)	Use
0	Liquid H_2	1.12 (Ave. first run)	
		1.37 (Ave. second run)	Target
1.3	Mylar	0.019	Target cell wall
5.1	Mylar	0.038	Target vacuum chamber
5.1	Air	~15	
23	Mylar	2×0.0064	P1 (PWC)
23	Aluminum	2×0.013	P1 (PWC)
23	Tungstun	0.0020 dia. (spaced 0.30)	P1 (PWC)
31	Mylar	2×0.005	SC4
31	Aluminum	5×0.001	SC4
33	Air	~76	
117	Mylar	2×0.005	SC5
117	Aluminum	9×0.005	SC5
132	Plastic scintillator	1.27	dE/dx
132	Aluminum	2×0.0025	dE/dx
132	Polyethelene	2×0.025	dE/dx
142	Lucite	5.1	Č
142	Aluminum	2×0.0025	Č
142	Polyethelene	2×0.025	Č
147	Brass	0.953	Range absorber
150	Plastic scintillator	0.635	P2
150	Aluminum	2×0.0025	P2
150	Polyethelene	2×0.025	P2
160	Mylar	0.013	Proton range chamber
165	Aluminum	0.152	First range-chamber plate
	Aluminum	2×0.475	Proton range-chamber plates
	Aluminum	10×0.635	Proton range-chamber plates
	Air, Ne	~168	Proton range-chamber plates

0.16 cm from the wires. A printed circuit board mounted on the frame of the chamber provided four separate channels, each with an amplifier, discriminator, and output circuit. The chamber was covered with aluminized Mylar to eliminate pickup problems, and an aluminum box covered the edges and the electronics. The chamber was run with a gas mixture of approximately 90% argon, 10% isobutane. With an applied voltage of 3.4 kV, a timing resolution of 50 nsec was achieved in coincidence with the other counters in the proton arm. The PWC functioned reliably for the various runs over a period of two years.

The dE/dx counter, of dimensions 61 cm×91.4 cm×1.27 cm, was coupled via twisted light pipes to a single 58AVP phototube on each end. The anode signals were mixed in order to measure the total output of the counter. This signal was sent to an ADC (analog-to-digital converter) in order to display dE/dx in digital form on film, and also to a PHA (pulse-height analyzer) in order to periodically check the pion-proton separation. Dynode signals from each tube were fed into a fast integration circuit which provided a pulse height approximately proportional to the total charge. This signal was amplified and provided the dE/dx part of the trigger. Typical values of dE/dx for stopping particles were 4.0 MeV/(g/cm^2) for 600-MeV/c protons and 2.0 MeV/(g/cm^2) for 100-MeV/c pions. The pulse height spread was ±15% for particles of 650 MeV/c. A Lucite Čerenkov counter provided further rejection against pions. This counter consisted of a Lucite block 50.8 cm×76.2 cm×5.08 cm viewed by four phototubes. The performance of the dE/dx and Čerenkov counters for particles stopping in the range chamber can be seen in Fig. 3.

For the first quarter of the experiment, the counter P2, which defined the recoil proton angles, was 38.1×91.4 cm, and resulted in an over-all trigger rate of 0.7 per 10^5 pions and a mass acceptance of 1.05 to 1.45 GeV/c^2. For the rest of the experiment, a 61 cm×91.4 cm counter was masked to 45.7 cm×91.4 cm with a 15.2 cm ×91.4 cm scintillation veto counter (designated P2A). This resulted in a trigger rate of 0.8 per 10^5 pions and a mass acceptance of 0.90 to 1.45 GeV/c^2. The veto counter P3, placed after the range chamber, was 91.4 cm wide by 122 cm high, and had a twisted light pipe on one side coupled to a single 58AVP phototube.

The forward arm consisted of three scintillation counters $\pi 1$, $\pi 2$, and $\pi 3$, which were used to detect one forward charged particle. The three scintillation counters were each 35.6 cm wide by 106 cm high, and were each coupled to a single 56DVP phototube via twisted light pipes. The geometry is shown in Fig. 2.

The spark chambers were pulsed on a master trigger signal which demanded an interacting beam pion, a stopping proton in the correct angular range, and a single charged particle entering the forward arm. The coincidence $\mathrm{B1 \cdot B2}$ indicated the total flux in the beam. The useful beam through the hole counter B3 and the hydrogen target as measured by the coincidence $\mathrm{B1 \cdot B2 \cdot \overline{B3}}$ was normally 88% of the $\mathrm{B1 \cdot B2}$ rate. $\mathrm{B1 \cdot B2 \cdot \overline{B3} \cdot \overline{B4}}$ indicated that a beam particle had interacted in the target. This rate was typically 1.4% of the $\mathrm{B1 \cdot B2 \cdot \overline{B3}}$ rate. The signature for a recoil stopping proton was $\mathrm{P1} \cdot dE/dx \cdot \overline{\check{\mathrm{C}}} \cdot \mathrm{P2} \cdot \overline{\mathrm{P2A}} \cdot \overline{\mathrm{P3}}$. The signature for a single charged particle in the forward arm consisted of one and only one pulse from either $\pi 1$, $\pi 2$, or $\pi 3$.

The master trigger signal gated off the logic, strobed the ADC and PHA, fired spark chambers, and triggered the slow logic. The slow logic provided signals which recorded the frame number and dE/dx on film, flashed fiducials on the chambers, advanced the cameras, and advanced a frame counter. A fast-gating circuit gated the logic during the 750-msec ZGS (Zero Gradient Synchrotron) beam spills and generated an event dead time. The dead time for most of the experiment was set at 100 msec, and resulted in only a a few percent loss of triggers. The delay in firing the spark chambers was approximately 400 nsec. The sensitive time of the chambers was made as short as practical in order to minimize the number of events in which multiple beam tracks appeared. The sensitive time of the beam chambers was adjusted so that for 400 nsec delay in the system, the single gap efficiency was better than 90%.

The beam, pion, and first two proton spark chambers were conventional thin aluminum foil chambers. The beam chambers had 4 gaps each and consisted of 0.0014-cm foils, stretched on 20.3-cm square aluminum frames, mounted inside a gas-tight box. The thin-foil proton chambers SC4 (4 gaps) and SC5 (6 gaps) were constructed with 0.0018-cm-thick aluminum foil stretched on 0.96-cm-thick Lucite frames, 20.3 cm square and 81.3 cm square, respectively. The pion chamber SC3 (8 gaps) consisted of 0.0025-cm-thick aluminum foils stretched on 86 cm square aluminum frames mounted inside a gas-tight box.

The range chamber consisted of 13 aluminum plates of dimensions 76.3 cm × 102 cm with one plate 0.15 cm thick, two plates 0.48 cm thick, and ten plates 0.64 cm thick. The plates were mounted inside a large aluminum-frame gas-tight box.

The shower chamber was constructed with 64 plates of 0.16-cm-thick stainless steel, 122 cm square, sandwiched between 0.79-cm-thick Lucite frames. The 5.5 radiation lengths of steel provided better than 99% conversion efficiency for γ rays from a few hundred MeV to 6 GeV, and the chamber could easily support four γ showers and a charged pion track. Four spark gaps with a common trigger gap were used to pulse the plates in four groups of sixteen gaps each.

D. Optics

Two cameras recorded the events. The "proton" film recorded the beam- and proton-arm spark chambers, while the "γ" film recorded the pion and shower chambers. The demagnification was about 70. Kodak 35-mm Shellburst film gave the required contrast, speed, and resolution.

The proton chambers, SC4 and SC5, were aligned so that they were photographed directly from the side, with the top view visible through a 45° mirror attached to the top of each chamber. The range chamber was handled in a similar manner, except that a field lens was necessary

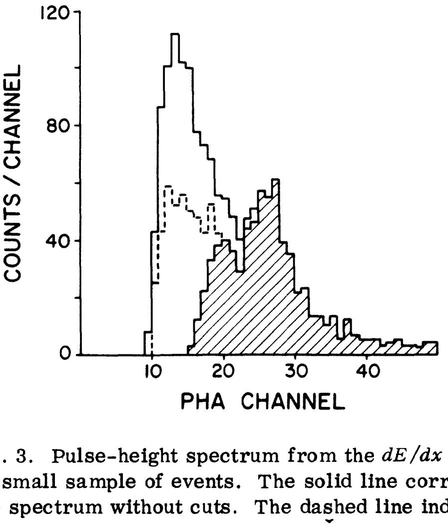

FIG. 3. Pulse-height spectrum from the dE/dx counter for a small sample of events. The solid line corresponds to the spectrum without cuts. The dashed line indicates the spectrum with the addition of the Čerenkov veto requirement, and the cross-hatched portion indicates the spectrum with both the dE/dx cut and the veto requirement.

for each view due to the large size and number of plates. The beam chambers SC1 and SC2, with their attached 45° mirrors, were viewed through one auxiliary mirror each, so that the images from these chambers appeared between those from SC3 and SC4 in the film format. Large 9.14-m-focal-length field lenses were used in conjunction with the forward arm. One lens in each view covered both the pion and shower chambers. Each view required two mirrors, and the resultant stereo angle was approximately 90°.

The fiducials for obtaining the reconstruction coefficients were of two types. Most were transparent crosses mounted on Lucite holders containing neon flash tubes. A total of 55 such fiducials were surveyed into position in several vertical survey planes located outside the spark chambers. Most of the fiducials were oriented such that their faces were approximately 45° to the vertical in order that they could simultaneously be seen in both views. All fiducials were activated by the master trigger and appeared on every frame. The beam chambers had additional fiducials of 5.08 cm separation cut on rectangular Lucite strips mounted inside the gas box, perpendicular to the chamber plates. A view of these fiducials had the same optical path as a view of the sparks. These fiducials were illuminated by dc lamps and recorded on a few frames of film at the beginning of each roll of film together with the pulsed fiducials.

The spark chambers and fiducials were surveyed into place each time the experiment was reinserted into the beam line. Checks of fiducials from one survey to the next, made before and after each run, typically agreed to within 0.025 cm. The beam chambers were removed at the end of each run in order to check the position of the beam hole-counter (B3) and the hydrogen target.

III. DATA ANALYSIS

A. Film scanning and measuring

The flow chart for the data analysis is given in Fig. 4. Film scanning for most of the experiment consisted of scanning only the "γ" film for the signature of two γ-ray showers within the shower chamber with a projected opening angle greater than 120 mrad in at least one view, and a straight track for the π^- beginning in SC3 and penetrating into the shower chamber. These frames and the corresponding proton frames were then measured. The cut in projected opening angle was based on the fact that the minimum opening angle for an η with a laboratory energy less than 6.0 GeV is about 180 mrad. By accepting only events with an angle greater than 120 mrad in at least one view, the scanners were able to reject $\pi^-\pi^0$ events. No $\eta\pi$ events were rejected by this opening-angle cut, and the number of events to be measured was reduced by a factor of about three. Events with an "old" beam track in the pion chamber, SC3, in addition to the pion track, were accepted because the pion-chamber sensitive time was somewhat greater than that of the beam chambers. It was found that only about 10% of the proton events associated with a good $\pi\gamma\gamma$ signature were unusable. Most of these failed due to either double beam tracks in the beam chambers, or proton interactions in the range chamber. The scanning efficiency for genuine $\pi\gamma\gamma$ events was determined to be $(75\pm5)\%$ by rescanning a subsample of the $\pi\gamma\gamma$ events at the three institutions where the scanning was done. In part, this scanning efficiency reflected the difficulty in scanning for low-energy showers.

The data were measured at the University of Toronto and the University of Wisconsin, mainly on image plane digitizers. Some fiducials and data were measured on film plane digitizers for comparison and distortion checks. The first and last spark of the tracks in both views of the chambers SC1, SC2, SC3, SC4, SC5 and the proton range chamber were measured, in addition to the first spark of the pion track seen in the shower chamber, and the first spark for each of the two γ conversions.

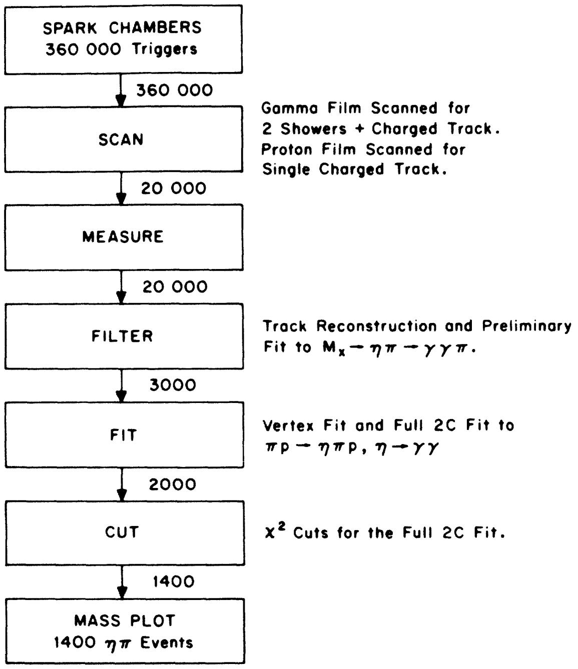

FIG. 4. Flow diagram for the processing of spark-chamber pictures.

B. Geometric reconstruction and kinematic fitting

A geometric reconstruction program, REK, was used to reconstruct measured spark positions in space using the measured data and a set of reconstruction coefficients derived from fiducial measurements and survey information.

In order to reduce the number of events requiring full kinematic reconstruction, a preliminary processing was performed. The beam and recoil proton information was used to calculate the four-momentum of the missing mass, which was then combined with the forward-arm track measurements to perform a pseudo-2C fit using fixed error estimates for the missing mass and $\pi\gamma\gamma$ tracks. A subroutine developed at the University of Winsonsin[22] fitted events to the $\eta\pi$ hypothesis as a preliminary event selection for filtering out most π^0 events. Rejection of events with $\chi^2 > 60$ for 2 degrees of freedom eliminated non-two-body decays and most $\pi^-\pi^0$ events while not biasing the $\eta\pi$ events. This preliminary fit reduced the number of events to be fully processed from 20 000 to 3000.

These preselected events were then reprocessed, and the reconstructed space points were fed into a series of subroutines which used a least-squares method based on that of Zacharov[23] to fit the beam, proton, and outgoing pion tracks to a unique vertex. This set of programs is called REKVTX. The point errors discussed in Sec. III E were used to generate the full error matrix for the subsequent kinematic fit. The bubble-chamber program SQUAW[24] was modified to deal with the data from this experiment. It uses a minimum χ^2 method to attempt a variety of kinematic fits, provides fully fitted momenta and angles for all tracks which satisfy the four energy-momentum constraint equations, and provides a fully correlated error matrix.

Kinematic fits tried by SQUAW were

(a) $\pi^-p \rightarrow \pi^-\gamma\gamma p$ (1C fit)

$$\text{(b)}\quad \left.\begin{matrix}\pi^-p\rightarrow\eta\pi^-p\\ \eta\rightarrow\gamma\gamma\end{matrix}\right\}\ \text{(2C fit)}.$$

C. Efficiency calculations

A Monte Carlo program was written to simulate the reaction $\pi^-p \rightarrow X^-p$, $X^- \rightarrow \eta\pi^-$, $\eta \rightarrow \gamma\gamma$. The results were used to give the phase-space spectrum needed for mass-spectrum fitting and the angular distribution efficiency.

When generating Monte Carlo events, the beam particle was assumed to be traveling parallel to the nominal beam line, but its interaction point was chosen randomly within the interaction region of the target. The beam momentum distribution was chosen to be flat between the limits of 5.95 and 6.02 GeV/c. The mass of the X^- was chosen using the phase-space distribution $d^2\sigma/dm^2dt = kq$, where k is a constant and q is the three-momentum of one of the decay particles in the rest frame of the X^-. The t distribution was input as $\exp(5t)$, which corresponds to the experimental result for the A_2 (see Sec. IV B). The proton momentum and polar angle were calculated from the values of the mass of the X^- and t. The proton azimuthal angle was chosen randomly within ± 20° relative to the horizontal plane. These two angles, together with the interaction points, specified the proton trajectory. The intersection of this trajectory with a plane representing the proton counter P2 was checked to see that it fell within the counter boundaries, and if not, the event was rejected.

The X^- events which passed the proton cut were allowed to decay isotropically in the c.m. system via $X^- \rightarrow \eta\pi^-$, $\eta \rightarrow \gamma\gamma$. Forward-arm detection cuts were applied to the events generated in this manner. The pion trajectory was checked to see if it passed within the chamber and counter boundaries. The γ's were allowed to convert in the shower chamber, and each conversion point was checked to see that it was far enough inside the chamber boundaries for the developing shower to be seen by a scanner. The effective edges of the γ chamber were determined from the experimental distribution of γ conversion points.

The mass spectrum of all events which passed the proton chamber boundary requirements was used as the phase-space function in the mass-fitting procedure. Comparison of this spectrum with that resulting from the forward-arm cut gives $f_0(M)$, the forward-arm detection efficiency. By using a $\cos^2\theta \sin^2\theta \sin^2\phi$ weighting function, the corresponding efficiency for a 2^+ decay, $f_2(M)$, was extracted. These functions are shown in Fig. 5. The Monte Carlo calculation for the angular distribution efficiency in the Gottfried-Jackson frame was subsequently used in fitting the angular distribution of the X^- decay.

D. π^-p elastic scattering

Pion-proton elastic scattering data were taken for calibration purposes at a beam momentum of 1.1 GeV/c. At this beam momentum, the proton angle and momentum are in the same region as they would be from the production of a 1.3-GeV/c^2 meson at a beam momentum of 6 GeV/c, and the outgoing pion is in approximately the same angular region as that of the pion from the $\eta\pi$ decay of such a meson. The elastic scattering data were fitted in several ways: fits ignoring the outgoing-pion mass and angle, 2C fits ignoring the outgoing-pion mass, and three different zero-constraint fits for the proton momentum. The use of these fits in the error analysis is discussed in Sec. III F and in Appendix A.

The kinematic fits of elastic scattering events give the correct pion-mass distribution only if the values of the angles for the charged particles, the momentum of the beam and proton, and the error matrix for the fit are all correct. This error matrix contains the information on the spark reconstruction errors, beam momentum resolution, proton momentum resolution, multiple scattering of charged particles, and fitted vertex error.

E. The treatment of errors in the geometric reconstruction

Although the mass resolution is dominated by the multiple scattering of the recoil proton, spark reconstruction errors, particularly on the outgoing pion and γ's, contribute to the mass resolution obtainable in a 2C fit to the $\eta\pi$ events. Such contributions must be accurately known to determine the mass resolution for the various fits that have been done. These values have been measured and checked for consistency in a variety of ways.

First, the reconstruction of points in real space was checked by reconstructing fiducial positions that were measured in the event format. The only difference between fiducial and spark reconstruction was the correction for the thick Lucite windows on SC4, SC5, and the shower chamber. The mean position of the fiducials, as given by the reconstruction, was typically within 0.018 cm of the survey positions on SC5, and within 0.038 cm on SC4 and the shower chamber. The internal fiducials on the beam chambers could not be seen in both views and could not be reconstructed directly, but extrapolations using the measured angles for viewing the chamber indicated that the reconstruction errors were less than 0.025 cm. The standard deviation of distributions for reconstructed fiducial positions was typically 0.025 cm.

Second, the statistical errors on spark reconstruction were determined by fitting straight lines to the four sparks measured on both the beam and proton trajectories, and the three sparks measured on the pion trajectory. The standard deviation errors for spark reconstruction were 0.038 cm for the beam, 0.064 cm for the proton, and 0.076 cm for the pion. The value of 0.064 cm for the proton track was confirmed by fitting a line to two sparks in each proton chamber separately and seeing how well it extrapolated to the target. There was a systematic correlation between the errors on the pion and γ conversion sparks and their position in SC3 and the shower chamber. The error variation with position in these chambers was not known to better than 0.064 cm, and the error could not be taken out with the reconstruction program. To handle the problem, the nominal statistical errors used in the track- and vertex-fitting program were set to 0.127 cm for the pion chamber, in which only a small part of the fiducial volume was used, and 0.178 cm for the shower chamber, in which all of the fiducial volume was used.

Third, vertex fits for elastic scattering and $\pi\gamma\gamma$ events provided a check of over-all track reconstruction independent of kinematical variables. Multiple scattering does not contribute significantly since most of the scattering occurs within a few centimeters of the vertex. The χ^2 probability distribution shown in Fig. 6 for the vertex fits of $\eta\pi$ events is basically flat with a small accumulation below 1% probability due to non-$\eta\pi$ events, and an accumulation near 100% probability presumably caused by the large nominal errors used to compensate for systematic effects in fitting the pion track. For the elastic scattering events, systematic errors cuased by the passage of the scattered pion through a section of chamber SC3 on only one side of the beam line (as discussed in Appendix A) resulted in a somewhat worse vertex fit than for the $\eta\pi$ events, and the χ^2 probability

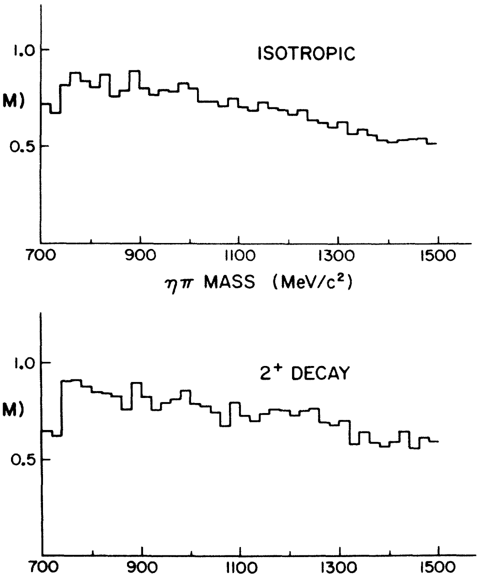

FIG. 5. The forward-arm detection efficiency as a function of $\eta\pi$ mass. The top histogram shows $f_0(M)$, obtained by using an isotropic decay angular distribution. The bottom histogram shows $f_2(M)$, which results from using the decay angular distribution $\cos^2\theta\ \sin^2\theta\ \sin^2\phi$ in the Gottfried-Jackson frame.

distribution has an accumulation at low probability. However, these errors are small and well understood. The error matrix in the reconstructed points was converted into an error matrix in fitted track angles by the program REKVTX and the associated vertex-fitting routines. The error matrix resulting from the vertex fit includes all the off-diagonal terms required to take into account the correlations between these angle errors.

F. Error analysis for the kinematic fitting procedure

The error matrix from the vertex fit was used as input to the kinematic fitting program SQUAW. To these angle errors must be added the errors in the beam and proton momenta and the additional errors in angle caused by the multiple scattering of the charged tracks. These are discussed in turn.

(i) The beam momentum. As discussed in Sec. IIA, the error in the 5.985 GeV/c beam momentum was taken to be 0.4%.

(ii) The recoil proton momentum. This error was determined to be 6 MeV/c from a knowledge of the stopping power of the plates in the range chamber and an analysis of πp elastic scattering at 1.1 GeV/c.

(iii) The multiple-scattering error. The mass resolution was dominated by the multiple-scattering error, primarily that of the proton. In the kinematic fitting procedure, the multiple-scattering error of the beam, the proton, and the outgoing pion was calculated for each event using the method of Gluckstern,[25] which includes contributions from small-angle single and plural scattering, scattering from the atomic electrons, and small-angle nuclear scattering. The errors calculated in this way were added in quadrature to the angle errors provided by the geometric reconstruction calculation.

Data obtained from the elastic scattering events were used to check this calculation by extracting a value for the multiple scattering contribution to the error in the beam-proton angle. Since these events are highly overconstrained, a value for the error in the proton momentum could be calculated (see Appendix A).

For these elastic scattering events, Monte Carlo studies, using the program LURCH, indicated that the beam momentum resolution at 1.1 GeV/c was 0.4%. Simple zero-constraint fits to the elastic scattering data, as well as 2C fits with SQUAW, gave a beam momentum resolution of 0.5% averaged over the various elastic scattering runs. This latter value was used in the analysis of the elastic scattering data.

The three zero-constraint fits for the elastic scattering proton momentum were consistent with each other, and gave a proton momentum resolution of 6 MeV/c, corresponding to an aluminum thickness of about half a plate in the proton range chamber. Using these values for the errors in the beam and proton momenta, the multiple-scattering error in the projected beam-proton angle was calculated to be 3.6 ± 0.6 mrad. This is in good agreement with the rms value of 3.8 mrad calculated in SQUAW for the $\eta\pi$ events (see Appendix A).

A stringent check on the accuracy of the error matrix used in the kinematic fits was obtained by consideration of histograms of the difference between measured and fitted quantities calculated by SQUAW. These histograms gave a measure of how far the measured variables had to be changed to satisfy the fit. These distributions for the fitted events should have a mean of zero and a unit standard deviation, if the input errors have been correctly estimated. For all the angles, for the beam and proton momenta, and for both the one-constraint fits to $\pi^- p \rightarrow \pi^- \gamma\gamma p$ and the 2C fits to $\pi^- p \rightarrow \eta\pi^- p$, $\eta \rightarrow \gamma\gamma$, these histograms had approximately Gaussian shapes with central values within three standard errors of zero, and standard deviations of approximately the expected value of 1. Finally, the χ^2 probability distribution for the 2C fits is shown in Fig. 7. Except for a small accumulation of events below 1% probability which are not considered to be $\eta\pi$ events, and a 3% excess accumulation below 5% probability, the distribution is flat, providing further confirmation that the errors were known well.

G. Mass resolution

The error in the determination of the invariant mass of any combination of final-state particles

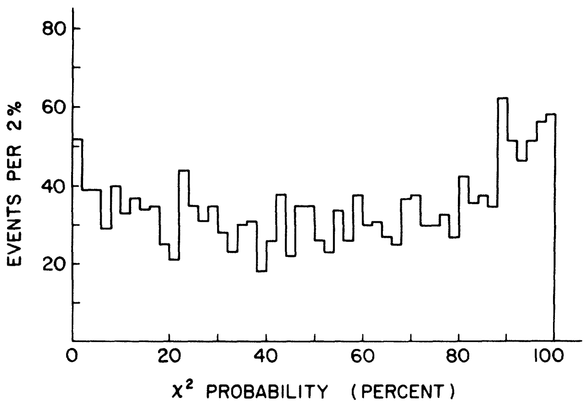

FIG. 6. χ^2 probability distribution for vertex fits of $\eta\pi$ events.

was calculated for each event by SQUAW using the error matrix in the final fitted quantities. The correctness of this procedure and of the errors which are used in this calculation could be conveniently checked in this experiment by using particles with zero natural width (the pion from the elastic scattering events and the π^0 and η from events which fit the reaction $\pi^- p \rightarrow \pi^- \gamma\gamma p$). A plot of the masses of these particles, assumed unknown and calculated by SQUAW, will have a nonzero width due to the errors discussed in the above Secs. IIIA-IIIF. The standard deviation of such a histogram should equal the root-mean-square error calculated for these events by SQUAW. (In actual fact, it is the histograms and errors of the square of the masses which are compared. For convenience, the results here have not been presented in this manner.) This type of analysis also provides a sensitive check on the estimated values of the point reconstruction errors of the γ conversion points from the π^0 and η decays.

The elastic scattering events were processed through the fitting programs using the error estimates discussed above, and assuming that the mass of the outgoing pion was unknown (Appendix A). The calculated mass spectrum for the resultant 2C fits fitted to a Gaussian distribution gave a mass value of 140.4 ± 1.3 MeV/c^2 with a standard deviation of 16.0 ± 1.0 MeV/c^2. The mean value of the distribution of the rms errors calculated for the events was 17 MeV/c^2. This value is in good agreement with the above value from the mass distribution itself.

The $\gamma\gamma$ mass spectrum from 1C fits to $\pi^- p \rightarrow \pi^- \gamma\gamma p$ is shown in Fig. 8 for a small sample of events which were not first processed by the preliminary fitting program that filters out most π^0 events. The π^0 mass was determined from the above distribution to be 135 ± 1 MeV/c^2 with a standard deviation of 9.0 ± 0.7 in good agreement with the calculated mean value of the rms errors of 9 ± 1 MeV/c^2 from SQUAW.

The $\gamma\gamma$ mass spectrum from one-constraint fits to $\pi^- p \rightarrow \pi^- \gamma\gamma p$ is shown in Fig. 9 for events which first passed the filter program. The central mass value is 549.6 MeV/c^2 with a standard deviation of 10.5 ± 0.5 MeV/c^2. The calculated rms error was 11.5 ± 0.5 MeV/c^2 excluding events with standard deviations greater than 25 MeV/c^2. The mass spectrum is not perfectly Gaussian in shape at the η mass, and would not be even if the expected error were the same for all events. The flat background peaks at the η mass after filtering, and there are systematic errors on reconstruction of some γ conversion points of about one standard deviation. Even so, the reasonable agreement of the observed η width with the calculated error indicates that the correct error mamatrix was used for reconstruction and kinematic fitting.

The $\eta\pi$ mass resolution for the 2C fit to $\pi^- p \rightarrow \eta\pi^- p$, $\eta \rightarrow \gamma\gamma$ was calculated for each event in SQUAW using the same fitted error matrix. The calculated resolution is different for each event primarily because of different proton and pion momenta, which give rise to different values of multiple-scattering errors. A histogram of the calculated rms errors is shown in Fig. 10 for all events which have a successful 2C fit. The distribution has a mean of 7.1 MeV/c^2, yielding a FWHM $\eta\pi$ mass resolution for the 2C fit of 16.7 ± 0.1 MeV/c^2. It is worth mentioning at this point that the mass resolution does not change by more than 10% over the range of proton momenta accepted, because the variation of mass resolution

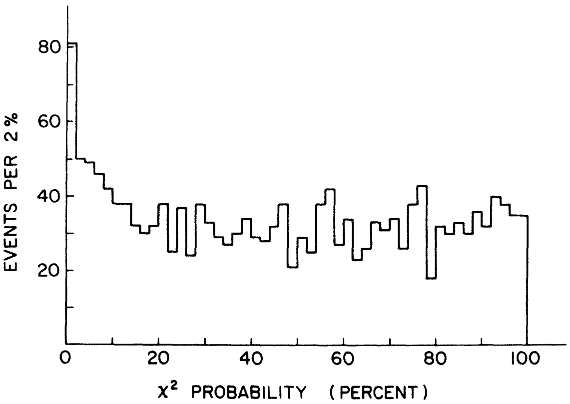

FIG. 7. χ^2 probability distribution for kinematic fits of events satisfying the hypothesis $\pi p \rightarrow \eta\pi p$, $\eta \rightarrow \gamma\gamma$.

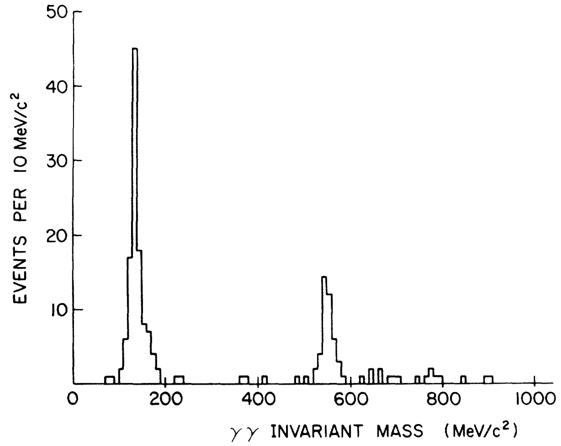

FIG. 8. The $\gamma\gamma$ invariant-mass spectrum for an unfiltered sample of events successfully fitted to the 1C hypothesis $\pi p \rightarrow \gamma\gamma\pi p$.

with proton momentum is determined more by the multiple scattering than by the kinematic partial derivatives. Therefore no advantage would be gained by deleting events not exactly in the Jacobian-peak region.

H. Background contribution to the η signal

The non-η background present in the final data was estimated from a small sample of events run through REKVTX and SQUAW without previous filtering (Sec. III B). As can be seen in the $\gamma\gamma$ mass spectrum from this sample (Fig. 8), there is no π^0 contamination of the η. It is expected that most of the non-η background is due to $\rho^-\pi^0$, with $\rho^- \to \pi^-\pi^0$, where one γ from each π^0 is seen. The non-η background from multi-π^0 events where only two γ rays are seen can be only crudely estimated from this small sample processed by SQUAW. Estimates from 2% to 12% can be obtained for various choices of background and width of the η signal.

To improve the determination of the background underneath the η peak, a version of REK was used to look at the $\gamma\gamma$ mass spectrum for a large sample of the measured events. The η was somewhat wider in this sample than in the SQUAW-processed events due to the poorer mass resolution. The non-η background in this latter data sample was estimated to be 5%.

Events with a calculated error in the $\gamma\gamma$ mass of greater than 40 MeV/c^2 have been rejected. In addition, the χ^2 probability from both the geometric (REKVTX) and kinematic (SQUAW) fits was required to be greater than 1%. At this point, a further restriction on the calculated $\eta\pi$ mass error to less than 15 MeV/c^2 had no effect.

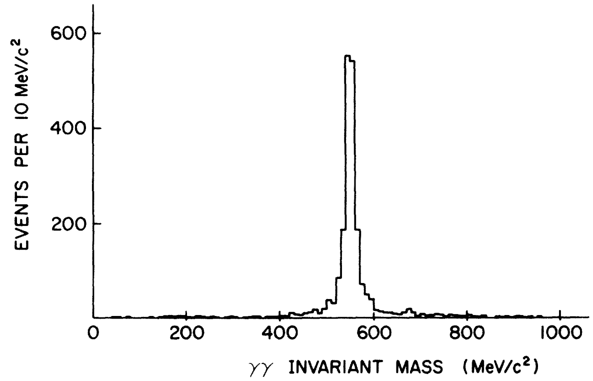

FIG. 9. The $\gamma\gamma$ invariant-mass spectrum for all events successfully fitted to the hypothesis $\pi p \to \gamma\gamma\pi p$ which have first passed through the filter routine.

I. The missing-mass measurement

As indicated in Sec. II D, all of the information for the beam pion and the proton was recorded on the same film. This made it possible to study the missing-mass spectrum from the reaction $\pi^- p \to X^- p$ in the region of the A_2, by measuring just the "proton" film from the 6.0-GeV/c run. The information on the errors gained from elastic scattering and $\eta\pi$ data using the forward arm provided a very good determination of the missing mass resolution. Since a large fraction of the "proton" film consisted of good protons, it was only necessary to measure about half of the "proton" film taken during the entire run to obtain the statistics necessary to resolve any double-peaked structure in the A_2 mass spectrum. The Wisconsin automatic measuring machine, SATR (semiautomatic track recognition), was used for most of this measurement and made the processing of such a quantity of film a relatively short project.

The missing-mass analysis was very similar to the CERN and the Northeastern–Stony Brook experiments in the choice of kinematic region, defined by the beam momentum of 6.0 GeV/c and the t range $0.27 \leq |t| \leq 0.42$ (GeV/c)^2. The trigger requirement was the same as in the $\eta\pi$ analysis so no separate discussion is given here. The only segment of the trigger which was different from other missing-mass experiments was the requirement of one and only one charged particle

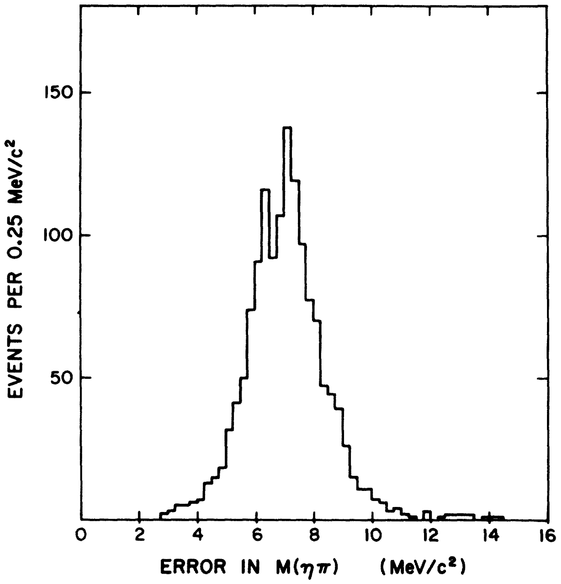

FIG. 10. Histogram of the $\eta\pi$ mass resolution (standard deviation) calculated for all events successfully fit to the 2C hypothesis $\pi p \to \eta\pi p$, $\eta \to \gamma\gamma$.

in the forward arm. The CERN experiment[3] tagged those events with multiple forward charged particles, while the other two Jacobian-peak experiments[10,11] did not include a forward-arm trigger requirement.

The selection of events was carried out in two stages: an "on-line" decision by the automatic measuring system computer or by the measurers for the hand-measured events, and a second cut applied at the analysis stage. The requirements for an event to be accepted for measurement were (a) one and only one track in the beam chambers SC1 and SC2, (b) one and only one track in the proton chambers SC4 and SC5, and (c) one track in the proton range chamber which was an approximate extension of the proton-chamber tracks. These selection criteria were somewhat more stringent than those used for the proton film in the $\eta\pi$ measuring in that events with no sparks in the range chamber were rejected. The major reasons for rejection of an event on film were multiple tracks in the beam chambers, no tracks in one view of a proton chamber, or no sparks in the proton range chamber. Approximately 45% of the pictures were accepted for measurement, and after the event selection by the reconstruction program about 45% of the measured sample remained, or about 20% of the frames scanned. (See Appendix B for details of the measurement of the missing-mass events.)

A total of about 172 000 pictures were processed, of which 134 000 were processed on SATR, 8000 on the manual measuring tables at Wisconsin, and 30 000 at the Rutherford High Energy Laboratory. Although the measuring errors for the hand-measured events were well known from studies of the $\eta\pi$ and elastic events, no such direct checks could be made on those events automatically measured. To monitor the errors in the film measured by SATR, a sample of elastic scattering events which had been measured on the manual tables was periodically measured on the SATR apparatus. An event-by-event comparison of the measurements showed that the measuring errors were similar for the two modes. Furthermore, there were no systematic shifts in either proton or beam angle or proton momentum, thus it was valid to combine events from the two modes. Of course, the missing-mass resolution is dominated not by the measuring errors, but rather by the multiple-scattering contribution. Finally, by measuring the same subsample of rolls of film a number of times, the reproducibility of the SATR event selection and measurement was checked. From these studies it was concluded that the only significant difference between SATR and hand-measured events was that SATR sometimes became confused by dirt or random sparks in the proton chambers, interpreting them as a second track. Therefore some good events were rejected by SATR, while a measurer could ignore such problems and accept the event. This slight discrepancy did not introduce any bias into the mass spectrum of the events chosen.

The results of Sec. III F were used to find the errors in the three quantities which contribute to the missing-mass resolution. These errors are as follows: (a) the beam momentum spread of 0.4%, (b) the recoil-proton-momentum associated error of 6 MeV/c, and (c) the proton scattering-angle error, dependent on proton momentum, with an average value of about 3.8 mrad. These three errors were used to calculate the mass resolution on an event-by-event basis for the missing-mass events. It was found that the resolution did not depend strongly on the proton momentum, but did vary with the mass, M_X. Figure 11 shows a plot of mass resolution vs missing mass, and it is seen that the total mass error at the A_2 peak is 10 MeV/c^2 (23.6 MeV/c^2 FWHM).

IV. RESULTS AND CONCLUSIONS

A. The $\eta\pi$ mass spectrum

The $\eta\pi$ mass spectrum for the 1400 events surviving all cuts is shown in Fig. 12. The estimates from the discussion of Sec. III H indicate that approximately 70 of the 1400 events are non-$\eta\pi$. The ηp and πp mass distributions for the same

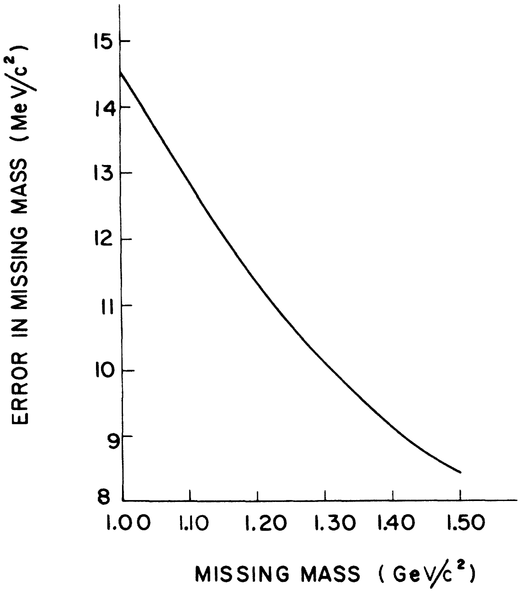

FIG. 11. Missing-mass resolution as a function of missing mass claculated from errors on the measured variables.

events are shown in Fig. 13. These distributions are heavily biased by the cuts on $\eta\pi$ mass and proton momentum, but indicate that there are no major biases of the $\eta\pi$ data due to ηp or πp resonances.

The $\eta\pi$ mass spectrum was fitted from 1.05 to 1.45 GeV/c^2 to the functional form $F_{\text{ps}}[af_0(M) + bf_2(M)F_{\text{BW}}]$. F_{ps} is the phase space for the production of two out of three bodies ($\eta\pi$ in the final state $\eta\pi p$) at a mass M, corrected for the t acceptance $0.27 \leqslant |t| \leqslant 0.42$ (GeV/c)^2. $f_l(M)$ is the geometric detection efficiency for an $\eta\pi$ system in a relative angular momentum state l, calculated using the Monte Carlo methods discussed in Sec. III C; $f_l(M)$ varies slowly with mass and is not dependent on t in this mass range.

The Breit-Wigner form used was

$$F_{\text{BW}} = \frac{MM_0\Gamma}{(M^2 - M_0^2)^2 + (M_0\Gamma)^2},$$

with $\Gamma = \Gamma_0(q/q_0)^{2l+1}\rho(q)/\rho(q_0)$. q (q_0) is the three-momentum of the η and π in the A_2 rest frame for a mass of M (M_0), l is the relative angular momentum between the η and π ($l = 2$), and $\rho(q) = (9 + 3R^2q^2 + R^4q^4)^{-1}$, with R, the radius of interaction, chosen to be $R^2 = 12$ GeV^{-2}. a, b, M_0, and Γ_0 are free parameters found by the minimum-χ^2 fitting procedure, which also includes the effect of a mass resolution of 7.1 MeV/c^2. This fit, shown with the data in Fig. 12, yields a mass $M_0 = 1.323 \pm 0.003$ GeV/c^2 and a width (corrected for resolution) of $\Gamma_0 = 0.108 \pm 0.009$ GeV/c^2 for the A_2, with a χ^2 of 38 for 36 degrees of freedom. It should be emphasized that the A_2 peak is accompanied by very little background. The background is about 7 events per 10-MeV/c^2 bin, of which it is estimated that less than 2 events per bin are not $\eta\pi$.

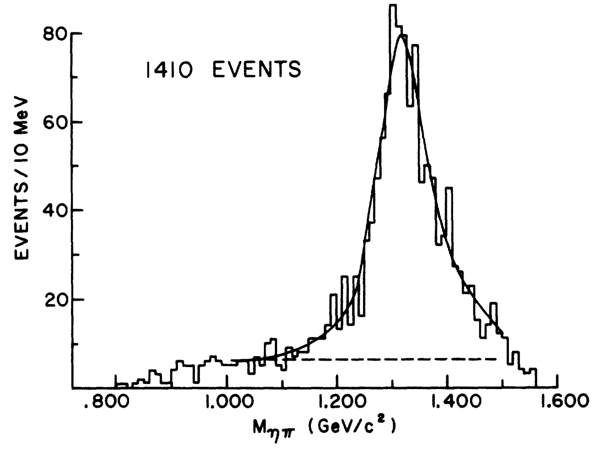

FIG. 12. Histogram of the $\eta\pi$ invariant-mass spectrum for the events surviving all the cuts detailed in the text.

The quoted errors are statistical only. The values of M_0 and Γ_0 are rather insensitive to the range of mass values covered in the fit, or to changes in the form of the phase space or efficiency functions. M_0 and Γ_0 deviated from the values quoted above by less than two standard deviations for all reasonable changes in the fitting functions which were tried [e.g., setting $f_0(M) = f_2(M) = 1$, ignoring the dependence of F_{ps} on t etc., and selecting a variety of mass ranges]. The results are also insensitive to the value of R^2. The systematic mass error is dominated by systematic errors in in the reconstructed spark positions. A consideration of possible sources of error from the surveying data and inclusion of smaller effects due to a possible systematic error in the beam and proton momenta lead to an estimated systematic mass error of less than 5 MeV/c^2.

The studies of the CERN MMS group[3] have suggested that the A_2 mass spectrum exhibits a so-called dipole shape of the form

$$F_{\text{DP}} = (M - M_0)^2/[(M - M_0)^2 + (\tfrac{1}{2}\Gamma_0)^2]^2 .$$

As might be expected from the data of Fig. 12, the $\eta\pi$ mass spectrum observed in this experiment is inconsistent with such a shape. In particular, a mass resolution of 7.1 MeV/c^2 and a dipole parameter $\Gamma_0 = 30$ MeV/c^2 would have given an observable valley-to-peak ratio of 0.5 in the present experiment.

There is no significant evidence for other resonances in the present t range from the $\eta\pi$ mass plot of Fig. 12. Half of the total $\pi\gamma\gamma$ data sample was used to study possible enhancements in the over-all $\gamma\gamma$ mass spectrum. The background

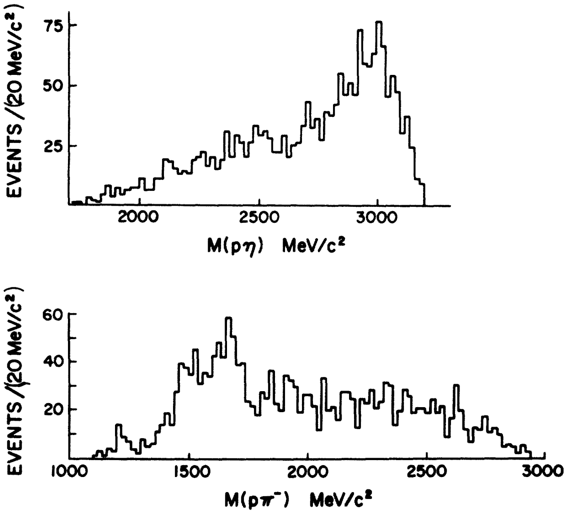

FIG. 13. The ηp and πp invariant-mass distributions for events of the type $\pi p \rightarrow \eta\pi p$, $\eta \rightarrow \gamma\gamma$ surviving the cuts detailed in the text.

level for this sample was about 6 events per 10-MeV/c^2 bin, with an estimated mass resolution of 20 MeV/c^2 FWHM. No unexpected effects are observed, and in particular, there is no evidence for $\eta'(958)\to\gamma\gamma$. Taking into account a reduced efficiency for η' detection due to the larger $\gamma\gamma$ opening angle, a two-standard-deviation upper limit to the branching ratio of $(A_2^-\to\eta'\pi^-\to\gamma\gamma\pi^-)/(A_2^-\to\eta\pi^-\to\gamma\gamma\pi^-)$ is about 3%. Using the relevant branching ratios yields a two-standard-deviation upper limit for the ratio $(A_2^-\to\eta'\pi^-/A_2^-\to\text{all})$ of about 6%.

B. Cross-section determination

It is difficult to extract an accurate value of the cross section for A_2 production from this experiment, since the cross-section determination depends upon a Monte Carlo calculation for the detection efficiency. Furthermore, the cross section integrated over all t depends upon the choice of the parameterization of the differential cross section. Keeping this in mind, the cross-section determination proceeds as follows.

The over-all detection efficiency for an $\eta\pi$ event, ϵ, depends upon a number of factors. Specifically,

$$\epsilon=\epsilon_{\Delta\phi}\,\epsilon_{\pi\gamma\gamma}\left(\frac{\eta\to\gamma\gamma}{\eta\to\text{all}}\right)\epsilon_{\text{misc}}$$

$\epsilon_{\Delta\phi}$, the average azimuthal efficiency for the proton arm, has the value $\epsilon_{\Delta\phi}=0.089\pm0.002$. $\epsilon_{\pi\gamma\gamma}$, the product of the $\pi\gamma\gamma$ forward-arm detection efficiency from a Monte Carlo calculation and the scanning efficiency for a $\pi\gamma\gamma$ event, has the value $\epsilon_{\pi\gamma\gamma}=0.38\pm0.05$. The quoted uncertainty (for $\epsilon_{\pi\gamma\gamma}$) represents a measured scanning efficiency uncertainty and a best estimate of the Monte Carlo uncertainty. $(\eta\to\gamma\gamma)/(\eta\to\text{all})$, the branching ratio for the η decay into $\gamma\gamma$, has the value 0.38 ± 0.01. ϵ_{misc}, a factor which includes a correction for the loss of good events due to double tracks in either the beam- or forward-arm spark chambers, a value for the trigger efficiency, and a correction for events lost by analysis cuts, has the value $\epsilon_{\text{misc}}=0.78\pm0.05$.

This leads to a value of the over-all efficiency of $\epsilon=(1.00\pm0.15)\times10^{-2}$ for detecting the final-state $p\eta\pi$ in the region of the A_2 mass for the t range $0.27\leq|t|\leq0.42$ $(\text{GeV}/c)^2$ at a beam momentum of 6.0 GeV/c.

The value of the differential cross section over the t acceptance of the experiment is then obtained by combining ϵ with the measured number of A_2 events, the beam normalization, and the protons/cm^2 in the hydrogen target. The $\eta\pi$ mass spectrum of Fig. 12 contains 1000 ± 40 A_2 events as determined by the Breit-Wigner fit described earlier. These considerations yield a value for the cross section $\Delta\sigma_{A_2\to\eta\pi}$ for $0.27\leq|t|\leq0.42$ $(\text{GeV}/c)^2$ of $\Delta\sigma_{A_2\to\eta\pi}=5.32\pm0.83$ μb. The mean value of the differential cross section over this t interval is $\langle d\sigma/dt_{A_2\to\eta\pi}\rangle_{\text{av}}=\Delta\sigma_{A_2\to\eta\pi}/\Delta t=35.5\pm5.5$ $\mu\text{b}/(\text{GeV}/c)^2$ at the mean value $\bar{t}=-0.34$ $(\text{GeV}/c)^2$. A branching ratio[18] of $(A_2\to\eta\pi)/(A_2\to\text{all})=0.153\pm0.013$ yields a value for the differential cross section $(d\sigma/dt)_{A_2\to\text{all}}=232\pm41$ $\mu\text{b}/(\text{GeV}/c)^2$.

Finally, a value for the cross section integrated over all t is obtained by using a differential cross-section parameterization of $d\sigma/dt=At'e^{Bt}$, with $B=6.41\pm0.33$ $(\text{GeV}/c)^{-2}$ determined by fitting data from 5 to 7.5 GeV/c $\pi^-p\to A_2^-p$ interactions.[26] An integration yields $(\Delta\sigma/\sigma)=0.25\pm0.01$, and thus $\sigma_{A_2\to\text{all}}=\Delta\sigma/(\Delta\sigma/\sigma)=137\pm25$ μb for the A_2 production via $\pi^-p\to A_2^-p$ at 6.0 GeV/c.

The value of $\langle d\sigma/dt_{A_2\to\text{all}}\rangle_{\text{av}}$ at $\bar{t}=-0.34$ $(\text{GeV}/c)^2$ obtained from this experiment is shown in Fig. 14 along with other $d\sigma/dt$ data obtained from the $A_2^-\to\rho\pi^-$ decay mode as compiled in the review paper of Michael.[27] The cross section as

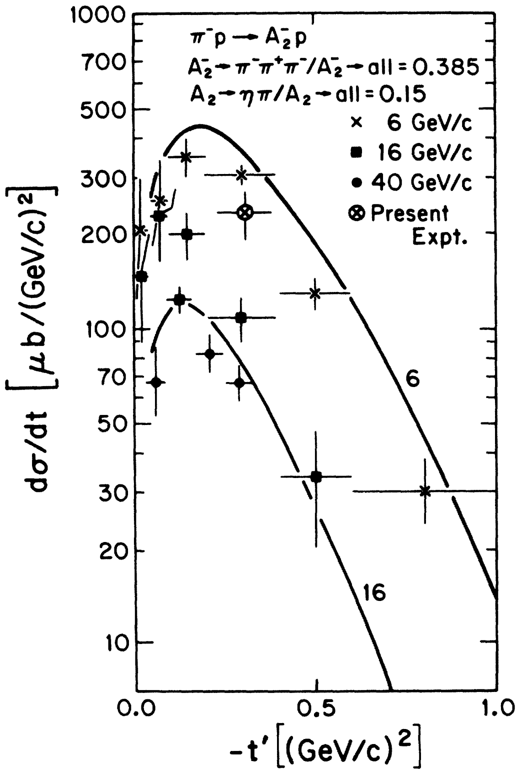

FIG. 14. The cross section $d\sigma/dt$ for the reaction $\pi^-p\to A_2^-p$ as obtained from the present experiment together with other cross-section measurements at various energies as compiled in Ref. 28 from the $A_2^-\to\pi^+\pi^-\pi^-$ decay mode. The solid curves represent a model calculation from Ref. 28 and are only included to show the trend of the data.

determined from the $\eta\pi$ decay mode in this experiment is in reasonable agreement with these data.

C. The angular distributions for the A_2

The angular distribution of events in the $\eta\pi$ mass plot of Fig. 12 between 1.21 and 1.43 GeV/c^2 has been studied in the Gottfried-Jackson (G-J) frame.[28] The histograms of $\cos\theta$ and ϕ for these events are presented in Fig. 15. Using the Breit-Wigner fit to the Fig. 12 mass spectrum, it is estimated that 150 of the 1020 events in this plot are background events. The possible spin and parity values of the A_2 decaying into $\eta\pi$ must be in the natural spin-parity series $J^P = 0^+, 1^-, 2^+, \ldots$. Although the data of Fig. 15 have not been corrected for the experimental efficiency, the histograms confirm that the A_2 has $J^P = 2^+$.

The decay angular distribution for a 2^+ meson decaying to two pseudoscalar mesons is given by[28]

$$\begin{aligned} W(\theta,\phi) = (15/16\pi)\{&3\rho_{00}(\cos^2\theta - \tfrac{1}{3})^2 + \rho_{11}(4\sin^2\theta\cos^2\theta) + \rho_{22}\sin^4\theta - \mathrm{Re}\rho_{21}(2\cos\phi\sin2\theta\sin^2\theta) \\ &- \mathrm{Re}\rho_{10}[2\sqrt{6}\cos\phi\sin2\theta(\cos^2\theta - \tfrac{1}{3})] - \rho_{1-1}(4\cos2\phi\sin^2\theta\cos^2\theta) \\ &+ \mathrm{Re}\rho_{20}[2\sqrt{6}\cos2\phi\sin^2\theta(\cos^2\theta - \tfrac{1}{3})] + \mathrm{Re}\rho_{2-1}(2\cos3\phi\sin^2\theta\sin2\theta) + \rho_{2-2}\cos4\phi\sin^4\theta\}, \end{aligned}$$

where the ρ_{ij} are the A_2 production density matrix elements. If the A_2 were produced by unnatural spin-parity exchange such as the η or B, ρ_{00} could be nonzero. If the A_2 were produced by natural spin-parity exchange, such as ρ or f^0, all ρ_{M0}, $|M| = 0, 1, 2$, would be identically zero. Previous experiments suggest that the A_2 production is dominated by natural spin-parity exchange with $\rho_{11} = \rho_{1-1} \cong \frac{1}{2}$.

In order to subtract the effects of the background, the nonresonant $\eta\pi$ events lying under the A_2 were assumed to consist of only S and P waves and thus to have a distribution $F_{\mathrm{BG}}(\theta,\phi) = K[1 + C(3\cos^2\theta - 1)]$, where C is a measure of the $\cos^2\theta$ component in the background. A fit of this function to the nonresonant events in the mass region 0.9 to 1.1 GeV/c^2 gives a value of $C = 0.25 \pm 0.15$. Since the background is small under the A_2, the fitted values of ρ_{ij} are rather insensitive to the value of C, and $C = 0.25$ has been assumed throughout the analysis.

The functions $W(\theta,\phi)$ and $F_{\mathrm{BG}}(\theta,\phi)$ were separately integrated over $\cos\theta$ and ϕ bins to yield a 20×20 matrix, and were added together in the ratio of A_2 mesons to nonresonant background given by the data. Each element of the matrix was then multiplied by the experimental angular efficiency calculated from the Monte Carlo programs described in Sec. III C, and the resulting values were projected onto the $\cos\theta$ and ϕ axes and normalized to compare with the raw data.

It should be noted that because of the different experimental efficiencies for the elements of this matrix, certain terms in $W(\theta,\phi)$ which might have been expected to be zero when the projections on the $\cos\theta$ or ϕ axes were made turned out in fact to have nonzero values. Fits were also made directly on the $\cos\theta$ versus ϕ scattergram. This method yielded the same values (within error) for the density matrix elements. The sensitivity to these values was about the same, while the statistical significance per bin was not as good.

The results of the least-squares fits yielding the density matrix elements are given in Table II. Quoted errors are purely statistical. $(\rho_{11} - \rho_{1-1})$ was used in the fit rather than ρ_{1-1} in order to simplify application of the constraint $(\rho_{11} - \rho_{1-1}) \geq 0$. It was also required that $\rho_{ij} \geq 0$, and the normalization condition was imposed by dividing all elements and errors by the trace of the matrix after the fit. The density matrix elements were obtained by three different fitting procedures. In fit 1, using all nine density matrix elements, all elements except ρ_{00}, ρ_{11}, and ρ_{1-1} are within one standard deviation of zero. In particular, since $\rho_{22} = 0.00 \pm 0.02$ and $|\rho_{2m}|^2 < |\rho_{22}||\rho_{mm}|$, all ρ_{2m} terms are expected to be consistent with zero. This leaves only one other term, $\mathrm{Re}\rho_{10}$, with a value of 0.07 ± 0.10. Fit 2, which included ρ_{00}, ρ_{11}, ρ_{1-1} and $\mathrm{Re}\rho_{10}$, gave a value of $\mathrm{Re}\rho_{10} = 0.07 \pm 0.05$. It should be noted that the term including $\mathrm{Re}\rho_{10}$ has an angular distribution which is very close to that of the experimental efficiency, and the value of this matrix element is thus very sensitive to uncertainties in the Monte Carlo results. Noting also that systematic errors are not included in the quoted error, it is apparent that the present data are consistent with $\mathrm{Re}\rho_{10} = 0$. $\mathrm{Re}\rho_{10}$ is set to zero in fit 3, yielding the values shown in Table II with no decrease in the χ^2 probability of the fit. The values in fit 3 are used to calculate the curves shown in Fig. 15. If the element ρ_{00} is set to zero, and a three-parameter fit using ρ_{11}, ρ_{1-1}, and $\mathrm{Re}\rho_{10}$ is made, an unacceptable χ^2 of 52 for 37 degrees of freedom is obtained. It appears that while $\mathrm{Re}\rho_{10}$ is not needed for an acceptable fit, a small amount of ρ_{00} very definitely is.

Contributions to the errors of the density matrix elements, in addition to the statistical errors calculated by the fitting procedure, are as follows:

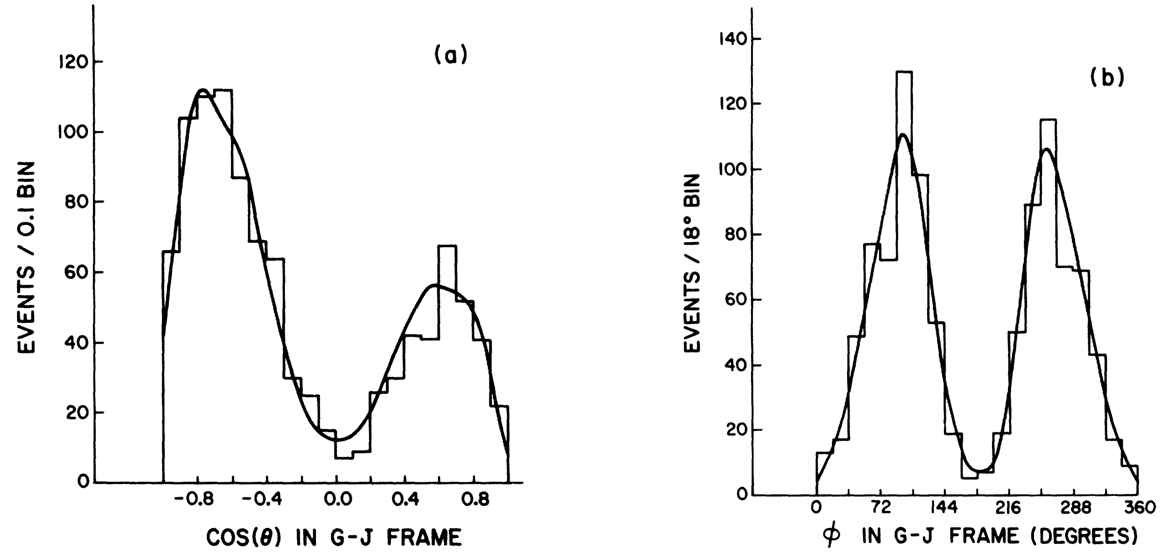

FIG. 15. (a) Distribution of $\cos\theta$ in the Gottfried-Jackson frame for the events with $1.21 \leq M(\eta\pi) \leq 1.43$ (GeV/c^2). The solid line is the result from a best fit to the angular distribution, corrected for the experimental detection efficiency. (b) The same for ϕ.

(i) The estimated error on the background of 150 events is ±30 events.

(ii) The error on the parameter C is ±0.15.

(iii) The error caused by the uncertainty in the angular dependence of the experimental efficiency was estimated by varying the boundary parameters in the Monte Carlo calculation.

By carrying out fits with the above values varied within their errors, estimates for the corresponding errors in the matrix elements were made. This procedure yielded errors of ±0.01 for ρ_{11}, ±0.03 for ρ_{00}, and ±0.04 for Reρ_{10}. The errors in parentheses in Table II for fits 2 and 3 represent the combined effect of these errors and the statistical errors.

It is clear from these results that A_2 production in this t range proceeds predominantly by natural spin-parity exchange with some small contribution from unnatural spin-parity exchange.

For comparison of these results with other ex-

TABLE II. Density matrix elements for the decay $A_2^- \rightarrow \eta\pi^-$ in the t range $0.27 \leq |t| \leq 0.42$ (GeV/c)^2 evaluated in the Gottfried-Jackson frame for the present experiment.

Fit	Density matrix element	Value	χ^2/D.F.[a]	Constraints
1	ρ_{00}	0.07 ± 0.05	34.7/31	None
	ρ_{11}	0.46 ± 0.10		
	$(\rho_{11} - \rho_{1-1})$	0.04 ± 0.26		
	Reρ_{10}	0.07 ± 0.10		
	ρ_{22}	0.00 ± 0.02		
	Reρ_{21}	0.03 ± 0.04		
	ρ_{20}	-0.01 ± 0.07		
	Reρ_{2-1}	-0.02 ± 0.03		
	ρ_{2-2}	-0.01 ± 0.09		
2	ρ_{00}	0.07 ± 0.03 (± 0.04)	41.8/36	All $\rho_{2m} = 0$
	ρ_{11}	0.47 ± 0.02 (± 0.02)		
	$(\rho_{11} - \rho_{1-1})$	0.00 ± 0.02 (± 0.03)		
	Reρ_{10}	0.07 ± 0.05 (± 0.07)		
3	ρ_{00}	0.09 ± 0.03 (± 0.04)	42.9/37	All $\rho_{2m} = 0$; Re$\rho_{10} = 0$
	ρ_{11}	0.45 ± 0.02 (± 0.02)		
	$(\rho_{11} - \rho_{1-1})$	0.00 ± 0.02 (± 0.03)		

[a] D.F. ≡ degrees of freedom.

periments, Table III (see Refs. 29–31) gives the density matrix elements from those experiments which have the best accuracy. The present results are quite consistent with the other experiments in this energy range. There is a strong indication that ρ_{00} tends to zero as the beam momentum increases, while ρ_{22} is consistent with zero in all experiments.

The problem of $\pi N \rightarrow A_2 N$ production mechanisms has been studied by Rosner[4] and by Michael and Ruuskanen.[32] They conclude that the dominant exchange is natural spin-parity, of which over 75% is isotopic singlet, probably f^0. The absence of any ρ_{22} is explained by Rosner using exchange-degeneracy arguments. The small amount of ρ_{00} is expected to be due to B, rather than η exchange, since the latter is suppressed by the small η-nucleon coupling constant. Fox and Hey[33] predict that the B-exchange part of the A_2 cross section falls off as p_L^{-2}, compared to the p_L^{-1} expected for f^0 exchange. This would tend to explain the decrease in ρ_{00} with higher energy.

In the study of the $\eta\pi$ mass spectrum obtained from a compilation of bubble-chamber data, Lacy[19] reported a significant fluctuation in the unnormalized interference-term density matrix elements R^{21}_{11} and R^{21}_{1-1}. $R^{JJ'}_{mm'}$ is the coefficient describing interference between a $|J,m\rangle$ state and a $|J',m'\rangle$ state and is defined in terms of the normalized density matrix element $\rho^{JJ'}_{mm'}$ by the relation

$$\rho^{JJ'}_{mm'} = R^{JJ'}_{mm'} \bigg/ \left[\sum_{m} (R^{JJ}_{mm})\right]^{1/2} \left[\sum_{m'} (R^{J'J'}_{m'm'})\right]^{1/2} .$$

The data in this compilation include about 150 A_2 mesons above background, and show that all but $\mathrm{Re}R^{21}_{11}$ and $\mathrm{Re}R^{21}_{2-1}$ are consistent with zero across the $\eta\pi$ mass range. However, both $\mathrm{Re}R^{21}_{11}$ and $\mathrm{Re}R^{21}_{1-1}$ show about a 2.5-standard-deviation difference from zero in the $\eta\pi$ mass range from 1.25 to 1.3 GeV/c^2, with $R^{21}_{11} = R^{21}_{1-1} = 0.2$. Lacy explained this fluctuation by postulating a resonant $J^P = 1^-$ state, with a mass of approximately 1.25 GeV/c^2, which could interfere with the $J^P = 2^+$ A_2.

In the present data, a fit to these interference terms over the mass range 1.05 to 1.45 GeV/c^2, using a method similar to that described above, indicates that all interference terms, except possibly R^{21}_{11} and R^{21}_{1-1} are consistent with zero. Assuming that R^{21}_{11} and R^{21}_{1-1} are the only nonzero terms, and demanding that they be equal, the values obtained for the entire A_2 region are $R^{21}_{11} = R^{21}_{1-1} = -0.027 \pm 0.012$. The fit has been repeated for 50-MeV/c^2 bins across the entire mass range. The results, given in Table IV, show that all values are consistent with zero, and, more importantly, no rapid fluctuation with mass of the sort reported by Lacy is observed.

Since the term containing R^{21}_{11} is odd for reflection in $\cos\theta$, small uncertainties in the Monte Carlo efficiency calculation have quite a sensitive effect on the values obtained, and the quoted errors are certainly underestimated. However, no reasonable variation of the Monte Carlo or fitting parameters can give a result in even moderate agreement with that of Lacy. The conclusion, from the present data, is that there is no evidence for any nonzero interference terms, or for any rapid variation in the values of these terms as a function of $\eta\pi$ mass.

D. The missing-mass result

The missing-mass spectrum in the mass range 1.00 to 1.45 GeV/c^2 is shown in Fig. 16. As discussed in Sec. III I, the missing-mass resolution was determined to be 10 MeV/c^2 (23.6 MeV/c^2

TABLE III. A compilation of the results of various experiments measuring A_2 density matrix elements.

P_L (GeV/c)	Reference	Observed decay mode	t range (GeV/c)^2	ρ_{00}	ρ_{11}	ρ_{22}	ρ_{1-1}
4	29	$K^-K^0_L$	0.12–0.72	0.24 ± 0.04	0.38 ± 0.04	0.00 ± 0.04	0.23 ± 0.04
4.5	30	$K^-K^0_S$	all	0.19 ± 0.05	0.34 ± 0.03	0.00	0.24 ± 0.04
5	31	$(3\pi)^-$	all	0.10 ± 0.05	0.43 ± 0.04	0.02 ± 0.05	0.35 ± 0.05
6	this exp.	$\eta^0\pi^-$	0.27–0.42	0.09 ± 0.04	0.45 ± 0.02	0.00 ± 0.02	0.45 ± 0.04
~7	19	$\eta^0\pi^-$	all	0.10 ± 0.13	0.42 ± 0.06	0.03 ± 0.06	0.43 ± 0.10
7.5	31	$(3\pi)^-$	all	0.06 ± 0.07	0.44 ± 0.05	0.03 ± 0.06	0.33 ± 0.07
11.2	31	$(3\pi)^-$	all	0.09 ± 0.10	0.41 ± 0.08	0.04 ± 0.08	0.41 ± 0.13
20.3	15	$K^-K^0_S$	0–0.1	0.11 ± 0.04	0.42 ± 0.02	0.03 ± 0.02	0.38 ± 0.03
20.3	15	$K^-K^0_S$	0.1–0.6	0.00 ± 0.01	0.47 ± 0.02	0.03 ± 0.02	0.46 ± 0.03

TABLE IV. The unnormalized interference density matrix elements for the decay $A_2^- \rightarrow \eta\pi^-$ as determined in the present experiment.

Mass range (GeV/c^2)	$R^{21}_{11} = R^{21}_{1-1}$
1.20–1.25	-0.008 ± 0.056
1.25–1.30	-0.039 ± 0.020
1.30–1.35	-0.013 ± 0.017
1.35–1.40	-0.033 ± 0.027
1.40–1.45	-0.041 ± 0.035

FWHM) at the A_2 peak, and was found to be mass-dependent, as shown in Fig. 11. The missing-mass spectrum in the mass range 1.00 to 1.45 GeV/c^2 has been fitted with several functional forms, each folded with a Gaussian resolution function whose width depends on mass. The spectrum was fitted to a D-wave Breit-Wigner form, using the equation $f(M) = Q(M) \times (a + F_{\text{BW}})$, where $Q(M)$ is a quadratic polynomial approximating a combination of phase-space terms (predominantly $\rho\pi$), and F_{BW} is the D-wave Breit-Wigner term. This fit is shown with the missing-mass spectrum in Fig. 16, which includes about 22 500 events of which about 6200 are in the A_2 peak. The mass and width values obtained are $M_0 = 1.324 \pm 0.003$ GeV/c^2 and $\Gamma_0 = 0.104 \pm 0.009$ GeV/c^2, with a χ^2 of 79 for 85 degrees of freedom. These values are consistent with the mass and width values obtained from the $\eta\pi$ decay mode, $M_0 = 1.323 \pm 0.003$ GeV/c^2 and $\Gamma_0 = 0.108 \pm 0.009$ GeV/c^2. The errors quoted are statistical only. The systematic mass error is estimated to be approximately 5 MeV/c^2. This systematic error combines the error in the mass scale and the errors caused by uncertainty in the background shape used in fitting the mass spectrum. It should be noted that the signal-to-background ratio for the missing-mass measurement is approximately unity at the A_2 peak, which is significantly better than other missing-mass experiments.

For comparison with other experiments a fit was made using an S-wave Breit-Wigner term plus a quadratic background, which yielded the parameters $M_0 = 1.319 \pm 0.002$ GeV/c^2 and $\Gamma_0 = 0.105 \pm 0.008$ GeV/c^2, with a χ^2 of 82 for 85 degrees of freedom. Finally, a fit to the data using a dipole form for the A_2 gives a confidence level of less than 10^{-5}. The dipole form used was $(M - M_0)^2 / [(M - M_0)^2 + (\frac{1}{2}\Gamma_0)^2]^2$, with M_0 and Γ_0 allowed to vary as free parameters of the fit. The resulting values were $M_0 = 1.319$ GeV/c^2 and $\Gamma_0 = 0.025$ GeV/c^2. The missing-mass spectrum was also divided into smaller regions of t within the acceptance interval. None of the subsamples so produced favored a dipole form.

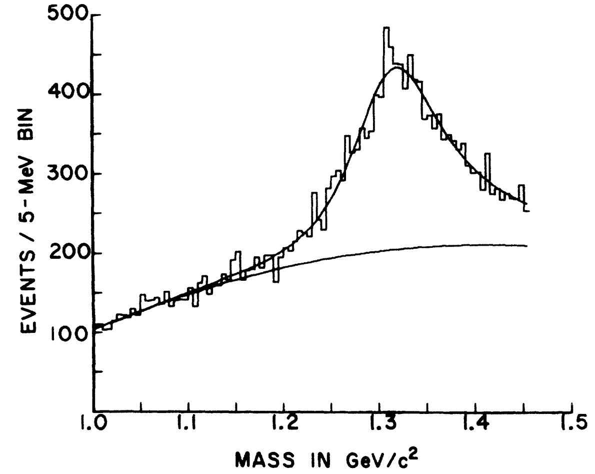

FIG. 16. Missing-mass spectrum from the present experiment for the reaction $\pi^- p \rightarrow X^- p$ at 6.0 GeV/c. The upper solid curve represents the Breit-Wigner form plus background, while the lower solid curve represents the background underneath the A_2.

ACKNOWLEDGMENTS

The support of B. Cork and the ZGS staff, particularly that of D. Cosgrove, F. Schweingruber, and R. Klem, is gratefully acknowledged. J. Gutman, D. Harrison, Y. Kwok, and C. Wuosmaa gave excellent assistance during the early parts of the experiment. D. Wiser helped run the experiment, supervise the measuring on SATR, and analyze the mass spectrum. It is also a pleasure to acknowledge the excellent work done by the scanning, measuring, and data-taking teams at the various institutions. At Toronto, Sheila Maggs provided general supervision, June Liu did an excellent job on the scanning, Quais Ashraf, Jim Bullard, and David Kesterton shared in the measuring, and Bruce Bolin and Shirley Scott were in charge of data processing. Scanning and measuring were also done at the University of Wisconsin, where particular thanks are due to the staff of SATR, M. Thompson, D. Brown, and V. Nelson. Thanks are also due to the scanning and measuring staffs at the Fermi National Accelerator Laboratory and the Rutherford High Energy Laboratory. Finally, we would like to thank J. Barney, E. Behr, Q. Kerns, G. Ott, and H. Petri for their participation in the design and construction of the apparatus.

APPENDIX A: ELASTIC SCATTERING

There are several advantages to using elastic scattering for calibration purposes. No changes in the apparatus, such as rotating spark chambers about the target, are necessary. The trigger is changed simply by deactivating the pion hodoscope counter $\pi 1$ nearest the beam to reduce accidentals. The coplanarity allows a consistency check of angular errors independent of momentum errors, assuming angular errors are the same in orthogonal directions.

There are several difficulties to be considered. Elastic scattering is not in a Jacobian peak; thus the proton momentum and angle errors are correlated, and these errors cannot be derived independently. However, they must be consistent with each other and with the angle errors for the $\eta\pi$ events, for which the momentum and angle errors are almost uncorrelated. The outgoing pion always scatters to one side of the beam in our geometry, and reconstruction errors that average to zero in the $\eta\pi$ events can produce systematic errors in the vertex and kinematic fits for the elastic scattering events.

The measured quantities used in the analysis of the 1.1-GeV/c elastic scattering data are P_0, the beam momentum; θ_p, the proton scattering angle; θ_π, the pion scattering angle; and P_R, the proton momentum as measured using the range chamber. In the first part of the analysis, the range measurement of the proton momentum was ignored. The proton momentum can be calculated using any two of the other three variables, and by subtracting $P_1(P_0, \theta_\pi)$, the momentum as calculated from P_0 and θ_π, from $P_2(P_0, \theta_p)$, that calculated from P_0 and θ_p, a distribution is obtained which should be centered at zero. The width of the distribution of $(P_1 - P_2)$ is related to the errors on P_0, θ_π, and θ_p by the formula

$$\sigma^2(P_1 - P_2) = \left[\sigma(\theta_\pi)\frac{\partial P_1}{\partial \theta_\pi}\right]^2 + \left[\sigma(\theta_p)\frac{\partial P_2}{\partial \theta_p}\right]^2 + \left[\sigma(P_0)\left(\frac{\partial P_1}{\partial P_0} - \frac{\partial P_2}{\partial P_0}\right)\right]^2 .$$

Since the errors on P_0 and θ_π are known, as are the partial derivatives, measuring the width of $(P_1 - P_2)$ allows extraction of the proton angle error to yield the value $\sigma(\theta_p) = 4.3 \pm 0.5$ mrad. By subtracting the contributions to this error due to measurement and reconstruction errors, which total about 2.0 mrad, the multiple-scattering error is calculated to be 3.8 ± 0.6 mrad. To compare with the data for 6.0-GeV/c running, a small correction must be made to account for the fact that the recoil protons have a higher average momentum, and thus a lower multiple-scattering value. This results in a multiple-scattering error of 3.6 ± 0.6 mrad, which is to be compared to the rms value of 3.8 mrad calculated in SQUAW using the Gluckstern formula.

Since the method of calculating P_1 and P_2 does not use the information from the range chamber, it is possible to use P_1 and P_2 as an independent measurement to check the range momentum. The distribution of $(P_R - P_1)$ should be centered at zero with a width given by

$$\sigma^2(P_R - P_1) = \sigma^2(P_R) + \left[\sigma(P_0)\frac{\partial P_1}{\partial P_0}\right]^2 + \left[\sigma(\theta_\pi)\frac{\partial P_1}{\partial \theta_\pi}\right]^2 .$$

An analysis of this distribution yielded a small correction to the parameter describing the amount of absorber through which the proton passed before reaching the range chamber and an estimated error in the absolute momentum calibration of less than about 2 MeV/c. Using the known errors in P_0 and θ_π, along with the measured width of $(P_R - P_1)$, the error in the range-momentum measurement was calculated to be $\sigma(P_R) = 5.8 \pm 0.5$ MeV/c.

Another check on the errors in proton angle and momentum was made by discarding the forward pion information and analyzing the events as missing-mass data. The Gaussian fit to the (missing mass)^2 distribution shown in Fig. 17 yields the parameters $\langle M_\pi{}^2\rangle = 0.0184 \pm 0.005$ (GeV/c^2)^2 and $\sigma(M_\pi{}^2) = 0.0071 \pm 0.0003$ (GeV/c^2)^2. The systematic error on the average value is estimated to be 0.0020 (GeV/c^2)^2. The expected value is $\langle M_\pi{}^2\rangle = 0.0194$ (GeV/c^2)^2, and the error $\langle M_\pi{}^2\rangle$, calculated from errors in P_0, θ_p, and P_R used above, is $\sigma = 0.008 \pm 0.001$ (GeV/c^2)^2, which is consistent with the measured value.

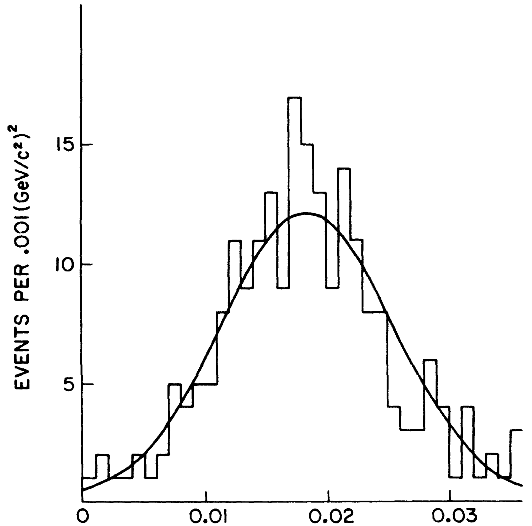

FIG. 17. The missing-mass-squared distribution for the elastic scattering events $\pi^- p \to \pi^- p$ at 1.1 GeV/c.

A final check was made by analyzing the elastic events with the vertex and kinematic fitting program, doing a two-constraint fit to the reaction $\pi^- p \rightarrow X^- p$. This method uses all of the measured quantities and their errors, but of course is not independent of the other methods used. A Gaussian fit to this mass spectrum yields a mass $M_0 = 140.4 \pm 1.3$ MeV/c^2 and $\sigma = 16.0 \pm 1.0$ MeV/c^2. The mass resolution, as calculated by SQUAW using the assigned errors on measured quantities, is 17 MeV/c^2, in good agreement with the measured σ.

APPENDIX B: MEASUREMENT OF MISSING-MASS EVENTS

The Wisconsin automated flying-spot measuring device, SATR, recorded several hits for a particle track (typically 6 hits per spark or spark gap). Consequently for each chamber view these hits were fitted to a straight line (track segment) and coordinates were generated for the intersection of that line with the two planes representing the outside extremes of the outer gaps of that chamber view. Such coordinates represented two "master" points per track per view, and were written on tape as part of the data record for that frame if the event was acceptable. Consequently, the event data format for the SATR events was identical with that for those events measured on tables.

Knowing the track segments in each thin-foil chamber view, on-line decisions were made at measuring time to ensure that the two track segments per stereo view were each portions of the same straight line (the "master" line for that stereo view). Events were accepted if they contained (a) one and only one track in the beam chambers SC1 and SC2, and (b) one and only one track in the proton chambers SC4 and SC5.

Additional requirements were placed on the proton track. The projection of the proton master line (for a stereo view) into the range chamber selected a fiducial area in that range-chamber view. Within that fiducial area there had to be at least one spark within the first four gaps for the event to be accepted. Identifying the proton track in the range chamber as being an extension of the track seen in the thin-foil chambers SC4 and SC5 was the most difficult aspect of the on-line software. Spurious sparks, or one or more gaps that did not fire, were the greatest source of possible confusion or grounds for rejection.

These measured events were reconstructed with the same reconstruction program used for the hand-measured events. This program rejected events if the four measured (master) points per stereo view from the thin-foil chambers for either the beam or the proton track did not form a straight line within tolerance, if the two tracks did not intersect, or if the intersection point did not lie within the target volume. Finally the program made a selection of events using the correlated information of dE/dx vs range for the particle in the proton arm. A scattergram of dE/dx pulse height vs range gap for a sample of events measured as missing-mass candidates showed a strong proton band with a weak pion band at low dE/dx. The collection of events following the reconstruction program had a pion contamination of some 25%, but most of this was in the region of low dE/dx and low range, and was easily rejected by a range-dependent dE/dx cut. This dE/dx cut reduced the fraction of pions in the proton sample to about 3%. After event selection by the reconstruction program, about 45% of the measured sample remained, or about 20% of the original frames processed.

In order to check for biases in on-line event selection, a frame-by-frame comparison was made on a sample of frames, comparing those events accepted (rejected) by SATR and those accepted (rejected) by a trained measurer. Finally, by measuring the same rolls of film a number of times on SATR, the reproducibility of event selection and measurement was checked. From these studies it was concluded that the only significant difference between SATR and hand-measured events was that SATR sometimes became confused by dirt or random sparks in the proton chambers, interpreting them as a second track. Therefore, it rejected a few good events where a measurer would accept them. The frequency of such discrepancies was small and should not have introduced any biases into the final mass spectrum.

---

†Work supported in part by the U. S. Atomic Energy Commission under Contract No. AT(11-1)-881-415.

*Now at Physics Department, University of Rochester, Rochester, N. Y. 14627.

‡Now at Istituto Nazionale di Fisica Nucleare, 00185 Rome, Italy.

§Now at City College of the City University of New York, New York, N.Y. 10532.

‖Now at Lawrence Berkeley Laboratory, Berkeley, Calif. 94720.

¶Now at Stanford Linear Accelerator Center, Stanford, Calif. 94305.

**Now at Princeton University, Department of Physics, Princeton, N. J. 08540.

[1] A. W. Key, G. Conforto, M. A. Kramer, D. G. Underwood, R. M. Mobley, R. Prepost, D. H. Tompkins, and M. S. Witherell, Phys. Rev. Lett. 30, 503 (1973). For additional details, see also D. G. Underwood, Ph.D. thesis, Department of Physics, University of Chicago, 1973 (unpublished).

[2] G. Conforto, M. A. Kramer, D. G. Underwood, R. M. Mobley, A. W. Key, R. Prepost, D. H. Tompkins, and M. S. Witherell, Phys. Lett. 45B, 154 (1973).

[3] B. Levrat, C. A. Tolstrup, P. Schübelin, C. Nef, M. Martin, D. C. Maglić, W. Kienzle, M. N. Focacci, L. Dubal, and G. Chikovani, Phys. Lett. 22, 714 (1966); G. Chikovani, M. N. Focacci, W. Kienzle, C. Lechanoine, B. Levrat, B. Maglić, M. Martin, P. Schübelin, L. Dubal, M. Fischer, P. Grieder, H. A. Neal, and C. Nef, Phys. Lett. 25B, 44 (1967).

[4] J. L. Rosner, in *Phenomenology in Particle Physics, 1971,* proceedings of the conference held at Caltech, 1971, edited by C. B. Chiu, G. C. Fox, and A. J. G. Hey (Caltech, Pasadena, 1971).

[5] H. Benz, G. E. Chikovani, G. Damgaard, M. N. Focacci, W. Kienzle, C. Lechanoine, M. Martin, C. Nef, P. Schübelin, R. Baud, B. Bosnjaković, J. Cotteron, R. Klanner, and A. Weitsch, Phys. Lett. 28B, 233 (1968).

[6] G. E. Chikovani, M. N. Focacci, W. Kienzle, U. Kruse, C. Lechanoine, M. Martin, and P. Schübelin, Phys. Lett. 28B, 526 (1969); R. Baud, H. Benz, B. Bosnjaković, D. R. Botterill, G. Damgaard, M. N. Focacci, W. Kienzle, R. Klanner, C. Lechanoine, M. Martin, C. Nef, V. Roinishvili, P. Schübelin, A. Weitsch, H. Blumenfeld, H. Jöstlein, and P. Lecomte, *ibid.* 31B, 401 (1970).

[7] R. Baud, H. Benz, B. Bosnjaković, D. R. Botterill, G. Damgaard, M. N. Focacci, W. Kienzle, R. Klanner, C. Lechanoine, M. Martin, C. Nef, V. Roinishvili, P. Schübelin, A. Weitsch, H. Blumenfeld, H. Jöstlein, and P. Lecomte, Phys. Lett. 31B, 397 (1970).

[8] R. Baud, H. Benz, B. Bosnjaković, D. R. Botterill, G. Damgaard, M. N. Focacci, W. Kienzle, R. Klanner, C. Lechanoine, M. Martin, C. Nef, V. Roinishvili, P. Schübelin, A. Weitsch, H. Blumenfeld, H. Jöstlein, and P. Lecomte, in *Experimental Meson Spectroscopy,* edited by Charles Baltay and Arthur H. Rosenfeld (Columbia Univ. Press, New York, 1970), p. 311.

[9] M. Alston-Garnjost, A. Barbaro-Galtieri, W. F. Buhl, S. E. Derenzo, L. D. Epperson, S. M. Flatté, J. H. Friedman, G. R. Lynch, R. L. Ott, S. D. Protopopescu, M. S. Rabin, and F. T. Solmitz, Phys. Lett. 33B, 607 (1970).

[10] D. Bowen, D. Earles, W. Faissler, D. Garelick, M. Gettner, M. Glaubman, B. Gottschalk, G. Lutz, J. Moromisato, E. I. Shibata, Y. W. Tang, E. Von Goeler, H. R. Blieden, G. Finocchiaro, J. Kirz, and R. Thun, Phys. Rev. Lett. 26, 1663 (1971).

[11] C. M. Ankenbrandt, B. B. Babson, R. R. Crittenden, R. M. Heinz, J. C. Krider, J. E. Mott, H. A. Neal, and A. J. Pawlicki, Phys. Rev. Lett. 29, 1688 (1972).

[12] D. M. Binnie, L. Camilleri, A. Duane, A. R. Faruqi, D. A. Garbutt, W. G. Jones, M. E. Kay, M. Lewis, P. J. Nicholson, I. Siotis, P. N. Upadhyay, J. C. Wilson, I. F. Burton, S. G. Frank, R. George, M. Haque, and J. C. McEwen, Phys. Lett. 36B, 257 (1971).

[13] D. M. Binnie, L. Camilleri, A. Duane, D. A. Garbutt, J. R. Holmes, W. H. Jones, J. Keyne, M. Lewis, I. Siotis, P. N. Upadhyay, I. F. Burton, R. George, and J. G. McEwen, Phys. Lett. 36B, 537 (1971). This experiment, which studied the reaction $\pi^- p \to A_2^- p$, $A_2 \to \pi^-$ +neutrals, reported some structure in the events produced at low values of t. This result apparently has been withdrawn (see Ref. 14).

[14] R. E. Diebold, in *Proceedings of the XVI International Conference on High Energy Physics, Chicago-Batavia, Ill., 1972,* edited by J. D. Jackson and A. Roberts (NAL, Batavia, Ill., 1973), Vol. 3, p. 41.

[15] K. J. Foley, W. A. Love, S. Ozaki, E. D. Platner, A. C. Saulys, E. H. Willen, and S. J. Lindenbaum, Phys. Rev. Lett. 26, 413 (1971); and Phys. Rev. D 6, 747 (1972).

[16] G. Grayer, B. Hyams, C. Jones, P. Schlein, W. Blum, H. Dietl, W. Koch, H. Lippmann, E. Lorenz, G. Lutjens, W. Manner, J. Meissburger, U. Stierlin, and P. Weilhammer, Phys. Lett. 34B, 333 (1971).

[17] See, e.g., R. Dalitz, in *Meson Spectroscopy,* edited by C. Baltay and A. H. Rosenfeld (W. A. Benjamin, Reading, Mass., 1968), p. 497.

[18] Particle Data Group, Rev. Mod. Phys. 45, 51 (1973).

[19] J. L. Lacy, Ph.D. thesis, Department of Physics, University of Illinois, 1971 (unpublished).

[20] M. S. Witherell, R. Prepost, D. H. Tompkins, G. Conforto, M. A. Kramer, D. Underwood, A. W. Key, and R. M. Mobley (unpublished).

[21] P. R. Bellinghausen and T. J. Lachance, Nucl. Inst. Methods 98, 269 (1972).

[22] R. Handler, Univ. of Wisconsin, private communication.

[23] B. Zacharov, Nucl. Inst. Methods 32, 163 (1965); H. J. Sherman, private communication.

[24] O. I. Dahl *et al.*, LBL Group A Programming Note, 1968 (unpublished).

[25] R. L. Gluckstern, Nucl. Inst. Methods 24, 381 (1963).

[26] U. E. Kruse, Univ. of Illinois Report No. C00-1195-234, 1972 (unpublished).

[27] C. Michael, in *Proceedings of the XVI International Conference on High Energy Physics, Chicago-Batavia, Ill., 1972,* edited by J. D. Jackson and A. Roberts (NAL, Batavia, Ill., 1973), Vol. 3, p. 165.

[28] K. Gottfried and J. D. Jackson, Nuovo Cimento 33, 309 (1964).

[29] C. M. Ankenbrandt, B. B. Brabson, R. R. Crittenden, R. M. Heinz, J. E. Mott, H. A. Neal, and A. J. Pawlicki, Phys. Rev. D 8, 2785 (1973).

[30] D. J. Crennell, H. A. Gordon, Kwan-Wu Lai, and J. M. Scarr, Phys. Lett. 35B, 185 (1971).

[31] G. Ascoli, D. V. Brockway, H. B. Crawley, L. B. Eisenstein, R. W. Hanft, M. L. Ioffredo, and U. E. Kruse, Phys. Rev. Lett. 25, 962 (1970).

[32] C. Michael and P. V. Ruuskanen, Phys. Lett. 35B, 47 (1971).

[33] G. C. Fox and A. J. G. Hey, Nucl. Phys. B56, 386 (1973).